Monthly Notices
of the
ROYAL ASTRONOMICAL SOCIETY

MNRAS **460,** 256–272 (2016)
Advance Access publication 2016 April 21

doi:10.1093/mnras/stw919

Recovering the tidal field in the projected galaxy distribution

David Alonso,[1⋆] Boryana Hadzhiyska[2⋆] and Michael A. Strauss[2⋆]

[1] *University of Oxford, Denys Wilkinson Building, Keble Road, Oxford OX1 3RH, UK*
[2] *Department of Astrophysical Sciences, Princeton University, Princeton, NJ 08544, USA*

Accepted 2016 April 15. Received 2016 April 8; in original form 2015 December 10

ABSTRACT

We present a method to recover and study the projected gravitational tidal forces from a galaxy survey containing little or no redshift information. The method and the physical interpretation of the recovered tidal maps as a tracer of the cosmic web are described in detail. We first apply the method to a simulated galaxy survey and study the accuracy with which the cosmic web can be recovered in the presence of different observational effects, showing that the projected tidal field can be estimated with reasonable precision over large regions of the sky. We then apply our method to the Two Micron All-Sky survey and present a publicly available full-sky map of the projected tidal forces in the local Universe. As an example of an application of these data, we further study the distribution of galaxy luminosities across the different elements of the cosmic web, finding that, while more luminous objects are found preferentially in the most dense environments, there is no further segregation by tidal environment.

Key words: cosmology: observations – large-scale structure of Universe.

1 INTRODUCTION

The nature of environmental effects in structure formation is an important field of study, both in astrophysics and cosmology. The dependence of halo and galaxy abundances on environmental density, for instance, gives rise to the bias relation linking the halo/galaxy distribution to the true matter density (Mo & White 1996; Sheth & Tormen 1999), and represents a central issue in the road to maximizing the amount of information that can be extracted from galaxy clustering analyses. Likewise, the environmental tidal forces are expected to distort the intrinsic shapes and alignments of galaxies, and therefore this effect must be correctly understood in order to obtain unbiased results from weak lensing studies (Catelan, Kamionkowski & Blandford 2001; Hirata & Seljak 2004).

Although the study of environmental effects has traditionally been focused on the impact of the environmental density, in recent years many groups have studied the effect of other quantities, such as the morphology of the environmental density field, the local tidal forces or the velocity field (Sousbie et al. 2008; Forero-Romero et al. 2009; Bond, Strauss & Cen 2010b; Hoffman et al. 2012). Each of these quantities can be used to define a different classification scheme of environment types in order to describe the statistics of the so-called 'cosmic web', i.e. the arrangement of the matter distribution into interconnected structures of different dimensionality (Bond & Myers 1996). Although the use of these additional observables undoubtedly furthers our understanding of environmental effects in structure formation, these quantities themselves may also contain relevant cosmological information.

There has been extensive work in quantifying and understanding the properties of the cosmic web from *N*-body simulations, as well as its interplay with various intrinsic halo and galaxy properties (Hahn et al. 2007; Kitaura et al. 2012; Yan, Fan & White 2013; Forero-Romero, Contreras & Padilla 2014; Libeskind et al. 2014; Nuza et al. 2014; Metuki et al. 2015), and a smaller number of groups have attempted similar studies on galaxy survey data (Bond, Strauss & Cen 2010a; Wang et al. 2012; Chen et al. 2015; Eardley et al. 2015). Often this is done by using the galaxy number density in redshift space as a proxy for the real-space matter density. However, this approach entails a number of difficulties, such as the theoretical uncertainty in the relationship between galaxies and dark matter or the presence of redshift-space distortions.

Furthermore, it is often difficult to measure accurate redshifts for a sufficiently large number of sources (e.g. very faint galaxies) and arguably the most practical solution to map the galaxy distribution at high redshifts and in large volumes is through the use of photometric redshifts. A number of photometric surveys, such as the on-going Dark Energy Survey (DES; The Dark Energy Survey Collaboration 2005), or the future Large Synoptic Survey Telescope (LSST) (LSST Collaboration et al. 2009) and the Euclid mission (Laureijs et al. 2011), have been designed to compile both deep and wide galaxy catalogues, covering large portions of the sky to redshifts $z \gtrsim 2$, and the analysis of these data will revolutionize our understanding of the cosmology and structure formation. Unfortunately, the lack of precise radial information in these surveys precludes any attempt at an accurate reconstruction of the 3D density field necessary to study the cosmic web. In these cases, however, there

⋆ E-mail: david.alonso@physics.ox.ac.uk (DA); boryanah@princeton.edu (BH); strauss@astro.princeton.edu (MAS)

is still a significant amount of information encoded in the projected 2D galaxy distribution, which could potentially be used to study the statistics of the cosmic web. Furthermore, there is evidence that the intrinsic alignment of galaxies (Blazek, McQuinn & Seljak 2011), a major contaminant to the weak lensing signal that these surveys hope to study, is heavily influenced by the dynamics of the projected tidal field (Catelan et al. 2001; Chisari et al. 2014), and therefore developing cosmic web analysis methods that work on 2D projected fields is of paramount importance. In this work, we present a method to carry out this kind of analysis, which we then implement on the Two Micron All-Sky Survey [2MASS hereafter (Skrutskie et al. 2006)], a low-redshift imaging catalogue, to produce a full-sky map of the projected tidal forces in the local Universe.

This paper is structured as follows. In section 2, we present our method as a 2D implementation of the cosmic web classification based on the tidal tensor, and interpret the recovered observable in terms of the projected transverse tidal forces. We validate this method in Section 3 by implementing it on an *N*-body-based synthetic galaxy catalogue, and devise a technique to deal with an incomplete sky coverage. The implementation of the method on the 2MASS survey is presented in Section 4. As a proof of concept, we also use the produced maps of the projected tidal field to study the dependence of the luminosity function (LF) on the tidal classification of the environment. Our conclusions are presented in Section 5.

2 THE 2D TIDAL TENSOR AND THE PROJECTED COSMIC WEB

2.1 The 3D tidal tensor

One of the most popular methods used in the literature to study the properties of the cosmic web is through the structure of the gravitational tidal forces (Doroshkevich 1970; Hahn et al. 2007; Forero-Romero et al. 2009). The action of these forces on an extended body of size $\boldsymbol{l}$ stretches or contracts it along different directions based on the structure of the Hessian of the gravitational potential $\bar{\Phi}$, also called the tidal tensor field:

$$\ddot{l}_i = -l_j\, \partial_j \partial_i \bar{\Phi}. \tag{1}$$

The tidal tensor is symmetric, and therefore can always be diagonalized at any point in space by performing a 3D rotation. The eigenvalues of the tidal tensor therefore inform us about the strength of the tidal forces in three independent orthogonal directions, and their sign can be used to classify four different types of environments. In the standard cosmic web classification, at a point in space in which all the eigenvalues are positive, extended objects will be compressed in all directions, and such a point is classified as a *knot*. On the other end, objects in a region where the tidal field has all-negative eigenvalues will be stretched in all directions, and the region is classified as a *void*. The intermediate cases correspond to filaments (two positive and one negative eigenvalues) and sheets (one positive and two negative eigenvalues).

Note that, even though this nomenclature alludes to the geometrical or morphological properties of these structures, the method is entirely based on the properties of the tidal field, and thus is dynamical in nature. This is different from the alternative approach of separating distinct elements of the cosmic web in terms of the morphology of the density field (e.g. Bond et al. 2010a). An added value of dynamical prescriptions is the direct physical interpretation of the resulting structures in terms of contracting and expanding directions, which can have a direct impact on the physics of galaxy formation. Other similar methods based on the tidal tensor or the velocity shear tensor have been proposed in the literature (Sousbie et al. 2008; Bond et al. 2010a; Hoffman et al. 2012; Libeskind et al. 2013) following a similar rationale.

Here, we will adhere to the formalism used in Forero-Romero et al. (2009) and Alonso, Eardley & Peacock (2015a). For simplicity, we will work with a rescaled version of the Newtonian potential: $\Phi \equiv \bar{\Phi}/(4\pi G\bar{\rho})$, for which the Poisson equation is simply $\nabla^2\Phi = \Delta$, where Δ is the matter overdensity field. We then define the tidal tensor field as $T_{ij} = \partial_i\partial_j\Phi$, so that $\Delta = \mathrm{Tr}(\hat{T})$, and we will classify the environment according to the number of eigenvalues α above a given threshold $\Lambda_{\rm th}$ (not necessarily $\Lambda_{\rm th} = 0$). The standard approach to compute the tidal tensor in 3D data sets is to first estimate the gravitational potential Φ by solving Poisson's equation in Fourier space, and then differentiate it (also in Fourier space) to compute its Hessian. Thus, the Fourier transforms of the tidal tensor and the 3D density field are related through

$$T_{ij}(\boldsymbol{k}) = \frac{k_i k_j}{k^2}\Delta(\boldsymbol{k}). \tag{2}$$

The density field used for these analyses is usually smoothed to a given scale R_s, either to mitigate shot noise, filter out non-linear effects or in order to study the scale-dependence of the resulting tidal field. We will do the same in the 2D case.

2.2 The 2D tidal tensor

2.2.1 *Definition*

The formalism introduced above is straightforward to implement in an *N*-body simulation, and methods have been devised to use it in spectroscopic galaxy catalogues as well (e.g. Bond et al. 2010b; Choi et al. 2010; Eardley et al. 2015), where 3D positions can be accurately determined for all galaxies (at least up to the effect of peculiar velocities). However, determining accurate spectroscopic redshifts for individual galaxies is a very time-consuming operation, and often in astronomy we are forced to make do with data sets for which radial positions are very poorly measured, as is the case for photometric redshift surveys, or even completely unknown. While a large amount of information is lost in the absence of accurate radial positions, a sizeable portion of it still remains encoded in the projected angular distribution of galaxies, at least for relatively shallow samples or those selected in a narrow range of photometric redshift. The method presented here is intended to enable the study of environmental tidal forces in the matter distribution in these cases.

The idea behind this method is to use a straightforward translation between 3D- and 2D-projected quantities. A proxy of the transverse components (i.e. perpendicular to the line of sight) of the projected tidal tensor is computed from the projected density field using the prescription as follows.

(i) The direct observable in a projected data set is the projected overdensity $\delta(\hat{\boldsymbol{n}})$: the fluctuations in the angular number density of galaxies with respect to the mean. This is related to the 3D overdensity field $\Delta(\boldsymbol{x})$ through a line-of-sight projection:

$$\delta(\hat{\boldsymbol{n}}) = \int_0^\infty \mathrm{d}\chi\; w(\chi)\,\Delta_{\rm s}(\chi\hat{\boldsymbol{n}}), \tag{3}$$

where χ is the comoving radial distance, $w(\chi)$ is the survey radial selection function and $\Delta_{\rm s}(\boldsymbol{x})$ is the redshift-space 3D overdensity field. Here and in what follows, we will denote all projected

quantities using the lower-case version of the symbols used for the analogous 3D objects.

As mentioned in the previous section, we filter out the smallest scales of the density field to mitigate shot-noise effects and non-linearities. For this we will use a Gaussian smoothing kernel defined by its standard deviation θ_s.

(ii) We define the *2D potential* ϕ as the solution to Poisson's equation on the sphere with δ as a source:

$$\nabla^2_{\hat{\boldsymbol{n}}}\phi \equiv \delta, \tag{4}$$

where $\nabla^2_{\hat{\boldsymbol{n}}} \equiv \partial^2_\theta + \partial^2_\varphi/\sin^2\theta + \cot\theta\partial_\theta$ is the covariant Laplacian on the sphere, and θ and φ are the elevation and azimuth spherical coordinates, respectively. Note that ϕ thus defined is not the same as the projected potential $\tilde{\phi}$, given by

$$\tilde{\phi}(\hat{\boldsymbol{n}}) \equiv \int_0^\infty \mathrm{d}\chi\; w(\chi)\,\Phi(\chi\hat{\boldsymbol{n}}). \tag{5}$$

We will discuss these differences in more detail in Sections 2.2.2, 3.3 and Appendix C.

(iii) The *2D tidal tensor* t_{ab} is then defined as the covariant Hessian of the 2D potential, $t_{ab} \equiv H_{ab}\,\phi$, where the covariant Hessian operator is given by

$$\hat{H} \equiv \begin{pmatrix} \partial^2_\theta & \partial_\theta(\partial_\varphi/\sin\theta) \\ \partial_\theta(\partial_\varphi/\sin\theta) & \partial^2_\varphi/\sin^2\theta + \cot\theta\partial_\theta \end{pmatrix}. \tag{6}$$

The procedure outlined above is a direct analogy with what is done to obtain the 3D tidal tensor: find the potential by solving Poisson's equation using Fourier methods and then compute the second derivatives of that potential. Although this is a simple way to define the 2D tidal tensor, we must first understand the physical interpretation of the object thus computed. We do so in the next section.

2.2.2 Physical interpretation of the 2D tidal tensor

The physical interpretation of the 2D tidal tensor introduced in the previous section is most easily understood in the flat-sky approximation. In this case, the projected overdensity is related to the 3D one through:

$$\delta(\boldsymbol{x}) \equiv \int \mathrm{d}z\; w(z)\Delta_s(\boldsymbol{x}, z). \tag{7}$$

Here, $\boldsymbol{x} = (x, y)$ are the coordinates perpendicular to the line of sight, and we have chosen z to be the radial coordinate. $\Delta_s(\boldsymbol{x}, z)$ is the 3D overdensity field in redshift space, and $w(z)$ is the radial selection function.

It is easy to relate $\delta(\boldsymbol{x})$ to the Fourier transform of the 3D matter overdensity field:

$$\delta(\boldsymbol{x}) = \int \frac{\mathrm{d}k^2}{2\pi} e^{i\boldsymbol{k}\boldsymbol{x}} \int \mathrm{d}q\; w(q)\, b\left[1 + \beta\frac{q^2}{k^2+q^2}\right]\Delta(\boldsymbol{k}, q), \tag{8}$$

where $\boldsymbol{k}$ and q are the components of the wave vector perpendicular and parallel to the line of sight, respectively, and $w(q)$ is the Fourier transform of the selection function

$$w(q) \equiv \int \frac{\mathrm{d}z}{\sqrt{2\pi}}\, w(z) e^{i\,qz}. \tag{9}$$

The factors b and β in equation (8) account for the galaxy bias and linear redshift-space distortions (i.e. $\beta \equiv f/b$, where $f \equiv d\log D/d\log a$ is the linear growth rate).

According to the definition used in the previous section, the 2D tidal tensor $\hat{t}$ and its 3D version $\hat{T}$ along the two transverse directions are related to the projected and 3D density fields in Fourier space, respectively, through

$$t_{ab} \equiv \frac{k_a k_b}{k^2}\delta(\boldsymbol{k}), \qquad T_{ab} \equiv \frac{k_a k_b}{k^2+q^2}\Delta(\boldsymbol{k}, q), \tag{10}$$

and thus, they are related to each other through

$$t_{ab}(\boldsymbol{x}) = b\int \frac{\mathrm{d}k^2}{2\pi} e^{i\boldsymbol{k}\boldsymbol{x}} \int \mathrm{d}q\;\omega(q,k)\,T_{ab}(\boldsymbol{k}, q), \tag{11}$$

where we have defined the modified selection function:

$$\omega(q,k) \equiv w(q)\left[1 + (1+\beta)\frac{q^2}{k^2}\right]. \tag{12}$$

On the other hand, the transverse components of the 3D tidal tensor projected along the line of sight are given by

$$\tilde{t}_{ab}(\boldsymbol{x}) \equiv \int \frac{\mathrm{d}k^2}{2\pi} e^{i\boldsymbol{k}\boldsymbol{x}} \int \mathrm{d}q\; w(q)\,T_{ab}(\boldsymbol{k}, q). \tag{13}$$

Comparing equations (11) and (13), we can see that the differences between the two quantities are fully encapsulated in the different selection functions w and ω.[1]

Typically, the selection function w of any survey will have a characteristic radial width l_z, and therefore its Fourier transform will have support over a range of scales $q \lesssim 1/l_z$ (e.g. the Fourier transform of a Gaussian selection function with variance l_z is a Gaussian with variance $1/l_z$). Since ω and w differ significantly only for values of $q \gtrsim k$ [we assume that the redshift-space distortions (RSD) parameter β is $O(1)$], this implies that, as long as we focus only on angular scales $k \gtrsim 1/l_z$, the 2D tidal tensor t_{ab} and the projected tidal tensor $\tilde{t}_{ab}$ will be proportional to each other to a very good approximation.

Hence, for sufficiently wide window functions, t_{ab} can be safely interpreted on all scales of interest as the magnitude of the tidal forces in the transverse directions averaged along the line of sight over the survey selection function. A more rigorous and quantitative proof of this result using a full-sky formalism is presented in Appendix C, and we demonstrate it in practice in Section 3.3.

2.2.3 Classification of the projected cosmic web

Bearing in mind the physical interpretation of the 2D tidal tensor, we can now justify an environmental classification based on it. We thus define three different types of environments in terms of the number of eigenvalues of the 2D tidal tensor larger than a given eigenvalue threshold $\lambda_{\rm th}$. We chose to retain the names *knots* and *voids* to denote regions in which both or none of the eigenvalues exceed the threshold, respectively, and we label any region in which only one of the eigenvalues is found above the threshold as a *nexus*. In what follows, we will order the two eigenvalues of the 2D tidal tensor have so that $\lambda_1 \geq \lambda_2$, and therefore our prescription for the tidal classification reads:

(i) *Void*: all eigenvalues below the threshold ($\lambda_1 \leq \lambda_{\rm th}$).

(ii) *Nexus*: only 1 eigenvalue above the threshold ($\lambda_2 \leq \lambda_{\rm th} < \lambda_1$).

(iii) *Knot*: all eigenvalues above the threshold ($\lambda_{\rm th} \leq \lambda_2$).

This formalism has one free parameter: the eigenvalue threshold $\lambda_{\rm th}$. In the 3D case, several prescriptions have been proposed in

[1] as well as the multiplicative galaxy bias factor b, due to the fact that the true tidal field is sourced by the total matter density.

the literature to choose a value for the analogous parameter $\Lambda_{\rm th}$. A choice of $\Lambda_{\rm th} = 0$ would separate different regions based purely on the direction of the tidal forces. This prescription would assume that gravitational collapse is underway along a given direction even if the eigenvalue is only infinitesimally positive, although in this case collapse would only occur after a very long time. This prescription thus produces a tidal classification in which voids occupy only about ∼20 per cent of the volume, in striking contrast with the visual impression from redshift surveys and *N*-body simulations that most of the volume is actually empty. A choice of $\Lambda_{\rm th} > 0$ would therefore only regard a given direction as 'collapsing' if the tidal forces are sufficiently strong, and would give rise to a tidal classification in which the abundance of voids better matches our intuitive expectations. The spherical collapse model would suggest an appropriate value for $\Lambda_{\rm th} \sim O(1)$ (Forero-Romero et al. 2009), which would actually classify a large fraction of regions with overdensities $\delta \gtrsim 1$ as voids. This is partly due to the failure of the spherical collapse model to describe the physics of anisotropic collapse, and therefore an intermediate value of $\Lambda_{\rm th}$ is sometimes chosen in order to produce the correct visual impression of the cosmic web classification.

In order to avoid this arbitrariness, we have followed a prescription similar to the one proposed by Eardley et al. (2015): for different values of the eigenvalue threshold, we calculate the number of galaxies in the survey located in the three different environmental types, and we choose the value of $\lambda_{\rm th}$ that most equally divides the galaxy population among the different types, thus minimizing the statistical uncertainty when studying the statistics of the galaxy population in all the environments simultaneously. The exact procedure we used to select a value for $\lambda_{\rm th}$ is the following: for the three environment types: ($\alpha = (0, 1, 2)$) we compute the fraction of galaxies in it: $F_\alpha = N_\alpha / N_{\rm total}$. We then compute the root-mean-square deviation in these fractions as

$$\Sigma_F = \frac{1}{3}\sqrt{\sum_{\alpha=0}^{2}\left(F_\alpha - \frac{1}{3}\right)^2}, \tag{14}$$

and select the value of $\lambda_{\rm th}$ that minimizes Σ_F. The actual value of $\lambda_{\rm th}$ depends on the smoothing scale used as well as on the galaxy population under study. As shown in Section 4.2, for our fiducial smoothing scale of 1° and the 2MASS sample, the optimal value is $\lambda_{\rm th} = 0.05$. Note that, although this criterion maximizes the statistics in the three environments simultaneously, it is not necessarily the optimal choice in order to enhance possible tidal effects in the galaxy distribution.

3 TESTING THE METHOD ON SIMULATED DATA SETS

3.1 Simulations

We have first tested the method to estimate the 2D tidal tensor on a simulated galaxy catalogue in order to rigorously verify the different systematic effects that could contaminate the measurements in the real data. The simulated data will also allow us to evaluate the agreement of these measurements with our theoretical expectations.

Our target galaxy catalogue is the 2MASS survey, described in Section 4.1, and therefore we generated the simulated catalogue to match 2MASS in terms of number density, clustering amplitude and redshift and magnitude distributions. The base of our simulated survey is a dark-matter-only *N*-body simulation, produced by the hybrid TreePM code GADGET-2 Springel (2005). It was run on a cubic box of size $L_{\rm box} = 700\,{\rm Mpc}\,h^{-1}$ containing 1024^3 particles with a particle mass $m_{\rm p} = 2.7 \times 10^{10}\,{\rm M}_\odot\,h^{-1}$. This mass resolution was necessary to populate the dark-matter haloes with galaxies matching the redshift and magnitude distributions of 2MASS. The simulation was run assuming a flat Λcold dark matter cosmology with cosmological parameters $(\Omega_M, \Omega_{\rm b}, h, \sigma_8, n_s) = (0.3, 0.05, 0.7, 0.8, 0.96)$, in approximate agreement with Planck Collaboration XVI (2014). The initial conditions for the simulation were generated at redshift $z_{\rm ini} = 49$ using second-order Lagrangian perturbation theory with a matter transfer function computed by the Boltzmann code CAMB (Lewis, Challinor & Lasenby 2000) for the cosmological parameters above.

A comoving snapshot of the simulation at redshift $z = 0.1$ (the median redshift of 2MASS) was used to generate the mock galaxy catalogue. First, a halo catalogue was generated using a Friends-of-Friends (FoF) code[2] with a linking length of $b = 0.2$ in units of the mean interparticle distance of the simulation. All haloes containing five or more particles were included in the catalogue.[3] Although it is not clear whether FoF groups with such a small number of particles can describe virialized structures accurately, the main aim of this catalogue is not to study the galaxy–halo relationship accurately, but rather to produce a galaxy sample that matches the statistical properties of 2MASS (Carretero et al. 2015), which we have managed to accomplish.

Haloes were populated with galaxies following a simplified version of the hybrid method proposed in Carretero et al. (2015), combining Halo Abundance Matching (Mo, Mao & White 1999; Vale & Ostriker 2004) and Halo Occupation Distribution (HOD; Peacock & Smith 2000; Berlind & Weinberg 2002) techniques. All haloes with masses larger than a threshold $M_{\rm min}$ were assigned a single central galaxy, and a mass-dependent average number of satellite galaxies given by (Jing, Mo & Börner 1998)

$$\langle N_{\rm sat}(M)\rangle = \left(\frac{M}{M_1}\right)^\beta, \tag{15}$$

and all haloes below $M_{\rm min}$ were left empty. The actual number of satellite galaxies assigned to each halo was drawn from a Poisson distribution with this mean. In order to assign luminosities to each galaxy following the 2MASS LF, we first related halo masses to luminosities by matching the cumulative LF and the cumulative galaxy number density as a function of halo mass. Specifically, halo masses ($M_{\rm h}$) were related to $K_{\rm s}$-band luminosities (L_K) by solving the equation:

$$\int_{L_K}^{\infty} {\rm d}L\,\frac{{\rm d}n_{\rm g}}{{\rm d}L} = \int_{M_{\rm h}}^{\infty} {\rm d}M\,n(M)[1 + \langle N_{\rm sat}(M)\rangle], \tag{16}$$

where ${\rm d}n_{\rm g}/{\rm d}L$ is the $K_{\rm s}$-band LF and $n(M)$ is the halo mass function. For the mass function, we chose the parametrization by Jenkins et al. (2001), which we found matches the halo mass distribution in our simulation to good accuracy. For the LF, we used the measurements of Appleby & Shafieloo (2014) at $K_{\rm s} < 13.5$, in which ${\rm d}n_{\rm g}/{\rm d}L$ is modelled as a Schechter function with parameters $\phi^* = 1.10 \times 10^{-2}\,({\rm Mpc}\,h^{-1})^{-3}$, $M_K^* = -23.52 + 5\log(h)$ and $\alpha = -1.00$.

Once the $M_{\rm h}$–L_K relation is found, central galaxies are assigned the luminosity corresponding to the host halo mass, and satellites

[2] The halo finder is publicly available and can be found at https://github.com/damonge/MatchMaker.

[3] Haloes with masses below five particles would only be necessary to reach survey completeness at $z \lesssim 0.03$, and omitting them has a negligible overall effect.

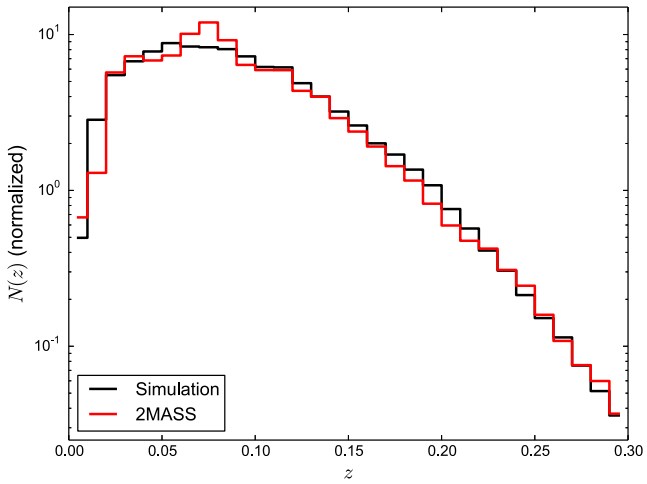

Figure 1. Redshift distribution of the simulated galaxy catalogue (black) and the sample of 2MASS galaxies with $K_s < 13.9$ used in this analysis (red). The latter was estimated from the redshifts of the complete spectroscopic sample in the northern galactic hemisphere, comprising ∼113 000 objects (see Section 4.2.3). Both histograms have been normalized to unit area.

are given a luminosity drawn from the satellite LF, given in its cumulative form by

$$n_{\rm sat}(>L_K) \equiv \int_{L_K}^{\infty} {\rm d}L\, \frac{{\rm d}n_{\rm g}}{{\rm d}L} - \int_{M_{\rm h}(L_K)}^{\infty} {\rm d}M\, n(M). \quad (17)$$

This algorithm guarantees that the resulting galaxy sample will follow the input LF. Once intrinsic luminosities were assigned, the apparent K_s magnitude was computed for each galaxy using equation (31), and a cut $K_s \geq 13.9$ (corresponding to the 2MASS completeness limit) was imposed.

The three free parameters of this method, $M_{\rm min}$, M_1 and β were fixed by matching the amplitude of the angular power spectrum in the simulation to that of the 2MASS data for three galaxy samples with different limiting magnitudes: $K_s < 13.5$, $K_s < 13.8$ and $K_s < 13.9$. We found the combination $\log_{10}[M_{\rm min}/({\rm M}_\odot\, h^{-1})] = 10.7$, $\log_{10}[M_1/({\rm M}_\odot\, h^{-1})] = 13.5$ and $\beta = 1.4$ to yield a good agreement with the data in terms of clustering amplitude, number density and redshift distribution.

Each galaxy was then given a cosmological redshift in terms of its comoving distance from the observer, which was further perturbed by the Doppler effect of its peculiar velocity to include the effect of redshift-space distortions.

Finally, we must note that the size of the simulation box is not quite large enough to encompass the whole volume covered by 2MASS. In order to achieve the required volume, we replicated the box once in each of the three dimensions, making use of the periodic boundary conditions of the simulation. This implies that our simulated catalogue lacks all clustering modes larger or similar to the size of the simulation box (700 Mpc h^{-1}), which is irrelevant for the scales used in the comparison of the mock catalogue with our 2MASS sample. The redshift distribution of our simulated catalogue is shown in Fig. 1 together with the corresponding one for 2MASS, extracted from the spectroscopic sample described in Section 4.2.3.

3.2 Statistics of the projected cosmic web

We first study the 2D tidal tensor and the projected cosmic web classification for the sample of galaxies in our simulated catalogue matching the fiducial sample used in the analysis of the 2MASS data, comprised of all galaxies with apparent magnitudes $K_s < 13.9$. For this sample we carry out the steps outlined in Section 2.2.1.

(i) Throughout the analysis we use the HEALPIX pixelization scheme (Górski et al. 2005) with a resolution parameter $N_{\rm side} = 64$, corresponding to pixels with an area of ∼0.84 deg^2. Given the number density of sources in 2MASS, higher resolution parameters would yield an estimate of the density field overly dominated by shot noise.

(ii) We compute the overdensity field in the full sky by counting the number of galaxies in each pixel $N_{\rm p}$ and dividing by the average number of galaxies per pixel $\bar{N}$. The field in pixel p is then given by

$$\delta_{\rm p} = \frac{N_{\rm p}}{\bar{N}} - 1. \quad (18)$$

(iii) Since our method to compute the 2D tidal tensor involves the numerical differentiation of the 2D potential ϕ, in order to suppress the numerical noise in the computation of those derivatives we first smooth the overdensity field using a Gaussian smoothing kernel, with standard deviation $\theta_{\rm sm} = 1^\circ$ and 5°. At the median redshift of our simulation ($\bar{z} \sim 0.08$), these angles correspond to physical scales of 4.4 and 31.2 Mpc h^{-1}, respectively. The use of different smoothing scales also allows us to study the properties of the cosmic web as a function of scale, which will be useful in order to compare our results with the linear theory outlined in Appendix B.

(iv) The 2D potential ϕ, as described by equation (4), is computed from the smoothed density field δ by solving Poisson's equation on the sphere. This is trivially done in harmonic space, since the harmonic coefficients of the two quantities are proportional to each other:

$$\phi_{\ell m} = -\frac{\delta_{\ell m}}{\ell(\ell+1)}. \quad (19)$$

(v) The 2D tidal tensor is then computed by differentiating the 2D potential as in equation (6). The covariant Hessian was computed using the routines provided by the HEALPIX PYTHON package `healpy`,[4] which perform the derivatives in harmonic space. The estimated tidal tensor in each pixel is then diagonalized, and the values of the two eigenvalues are used to classify each pixel as belonging to one of the three environments defined in Section 2.2.3 (void, nexus and knot) for a given eigenvalue threshold $\lambda_{\rm th}$.

Fig. 2 shows the main products of this process. The top-left panel shows a full-sky map of the density field smoothed with a 1° kernel used to infer the 2D tidal tensor. The environment classification derived from this tidal tensor, using the fiducial eigenvalue threshold quoted in Section 4.2 is shown in the top-right panel. Finally, the two bottom panels show full-sky maps of the two eigenvalues of the 2D tidal tensor.

For this data set, Fig. 3 shows the fraction of the sky classified as each of the three environments as a function of the eigenvalue threshold $\lambda_{\rm th}$ for 1° (left-hand panel) and 5° (right-hand panel) Gaussian smoothing kernels. The figure also shows the prediction from Gaussian theory outlined in Appendix B in both cases. The 1°-smoothed density field is clearly non-Gaussian and therefore the sky fractions are only in rough agreement with the Gaussian theory. After filtering out the smallest scales, responsible for most of the non-Gaussianity, we find that the Gaussian theory is able to describe the statistics of the projected cosmic web reasonably well for the 5°-smoothed field.

[4] https://healpy.readthedocs.org/en/latest/

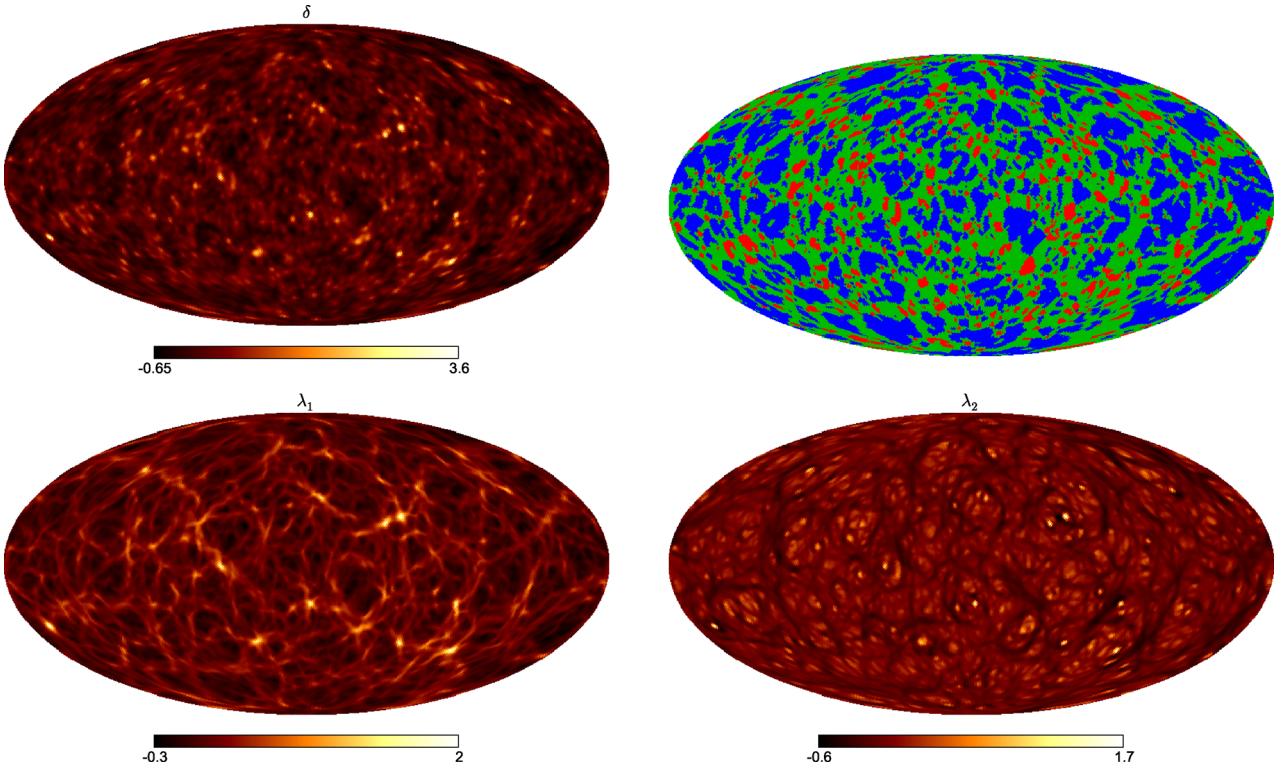

Figure 2. Top left panel: density field of the simulated galaxy catalogue smoothed with a 1° Gaussian kernel. Top right panel: environment classification for the fiducial threshold $\lambda_{\rm th} = 0.05$, with knots, nexuses and voids shown in red, green and blue, respectively. Bottom panels: full-sky maps of the two eigenvalues of the 2D tidal tensor.

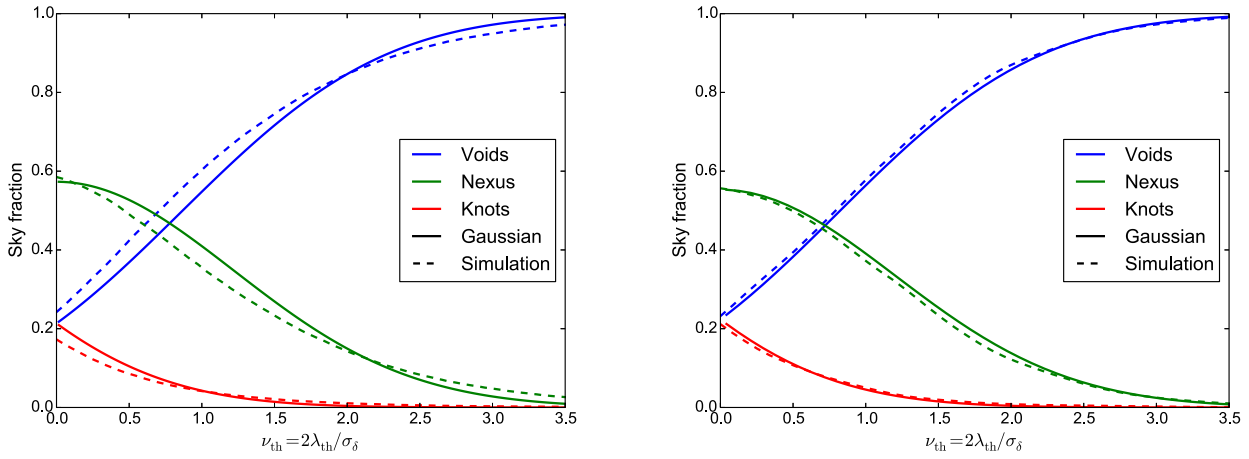

Figure 3. Gaussian prediction for the sky fraction each environment occupies as a function of the ratio of the eigenvalue threshold and the standard deviation of the projected overdensity field (solid), compared with the sky fractions in the simulated data (dashed). The smoothing angle is $\theta_{\rm sm} = 1^\circ$ for the left-hand panel and $\theta_{\rm sm} = 5^\circ$ for the right one. The effects of non-linearities are significantly reduced for the larger smoothing scale, and the measured sky fractions agree better with the Gaussian prediction.

3.3 Connection with the projected tidal field

It is important to verify the degree to which the 2D tidal field is a good representation of the true underlying projected tidal forces. The latter quantity, once projection effects are correctly modelled, can be used as a morphological probe of the matter density field and, as was mentioned in Section 1, is thought to have a large impact in the intrinsic alignment of projected galaxy shapes.

In Section 2.2.2 and Appendix C, we have provided analytical evidence that the connection between these two quantities is sound. However, using the true matter distribution available in the *N*-body simulation used to generate our mock galaxy catalogue, we can carry this comparison further by taking into account all the details of non-linear structure formation. As a bonus, this will also allow us to study the connection between the 2D tidal field and the true 3D tidal forces (i.e. in the absence of projection effects). In order to do this, we have carried out the following exercise.

(i) We first construct the 3D density field of the simulation by interpolating the matter particles on to a Cartesian grid using cloud-in-cell interpolation. This was done using a grid with 512 grid points per dimension, corresponding to a resolution $\Delta x = 1.37\,{\rm Mpc}\,h^{-1}$.

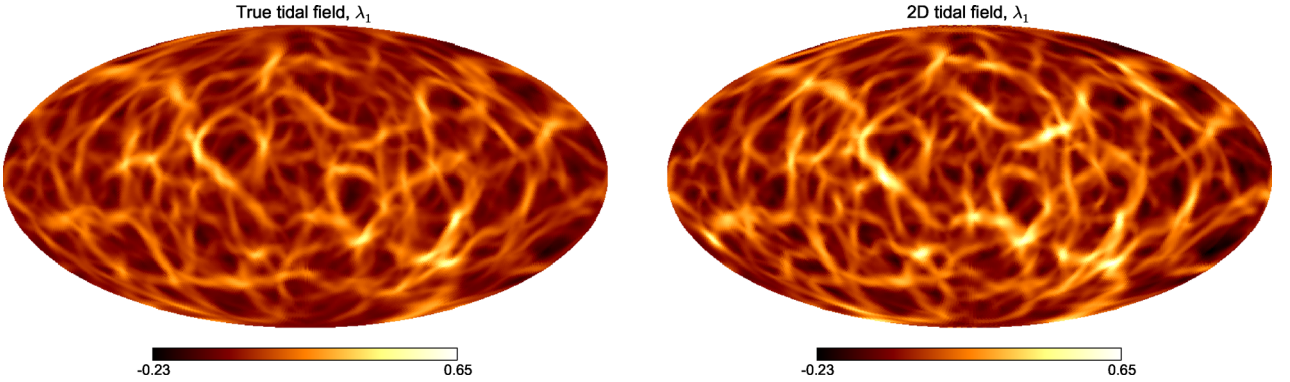

Figure 4. Left panel: principal eigenvalue of the true projected tidal field in our N-body simulation. Right panel: principal eigenvalue of the 2D tidal field measured from the corresponding mock galaxy catalogue. A Gaussian smoothing kernel with $\theta_s = 2^\circ$ was used in both cases. As discussed in Section 2.2.2, the 2D tidal field can be interpreted as a biased version of the true projected tidal field for most scales of interest.

We replicate this density grid in the three dimensions as described in section 3.1 to cover the volume of 2MASS.

(ii) At each grid point, we compute the value of the 3D tidal field by inverting Poisson's equation. Then, placing the observer at the centre of the simulated volume, we compute the transverse (angular) components of the 3D tidal field, as defined by the observer, by performing the corresponding 3D rotation.

(iii) We define a number N_z of angular pixel maps at different redshifts sampling the volume covered by 2MASS. For this we used $N_z = 1024$ maps uniformly distributed in the range $z \in [0, 0.3]$, each of them with an angular resolution HEALPIX parameter $N_{\rm side} = 1024$. The values of T_{ab} computed in the Cartesian grid are then interpolated on to these spherical maps using trilinear interpolation. The high angular and radial resolution of the maps ($\Delta x_\parallel \simeq 0.82\,{\rm Mpc}\,h^{-1}$, $\Delta x_\perp < 0.8\,{\rm Mpc}\,h^{-1}$) guarantees that essentially no information is lost in the process.

(iv) The projected tidal tensor is then estimated by performing a weighted average over the N_z maps with weights corresponding to the survey redshift distribution:

$$\hat{\hat{t}}_{\rm p} = \frac{\sum_{i=1}^{N_z} n(z_i)\,\hat{T}_{\rm p}^{(i)}}{\sum_{i=1}^{N_z} n(z_i)}, \tag{20}$$

where $\hat{T}_{\rm p}^{(i)}$ are the transverse components of the 3D tidal tensor in the i-th pixel map at pixel p, and $n(z_i)$ is the number of galaxies found in the i-th redshift bin.

The projected tidal field thus computed can then be compared with the 2D tidal tensor estimated from the mock galaxy catalogue as described in section 3.2. Fig. 4 shows the full-sky maps of the largest eigenvalue of both tensors for a smoothing scale $\theta_{\rm sm} = 2^\circ$. The result supports the physical interpretation described in Section 2.2.2: at most scales of interest the 2D tidal tensor is a biased representation of the projected tidal forces, with the bias factor given by the bias of the galaxy sample used to compute it.

In order to demonstrate this quantitatively, we have carried out the following exercise: we first compare the values of the projected galaxy overdensity field $\delta_{\rm g}$ and the true projected matter overdensity $\delta_{\rm M}$, computed by averaging the 3D matter overdensity in the simulation along the line of sight. From these data, we estimate the density bias b_δ by fitting a linear model $\delta_{\rm g} = b_\delta\,\delta_{\rm M}$, finding a best-fitting value $b_\delta = 1.15$ with a correlation coefficient $r = 0.9$. We then rescale the principal eigenvalue of the 2D tidal tensor in the simulation by b_δ and compare the result with the principal eigenvalue of the true projected tidal tensor computed as described above.

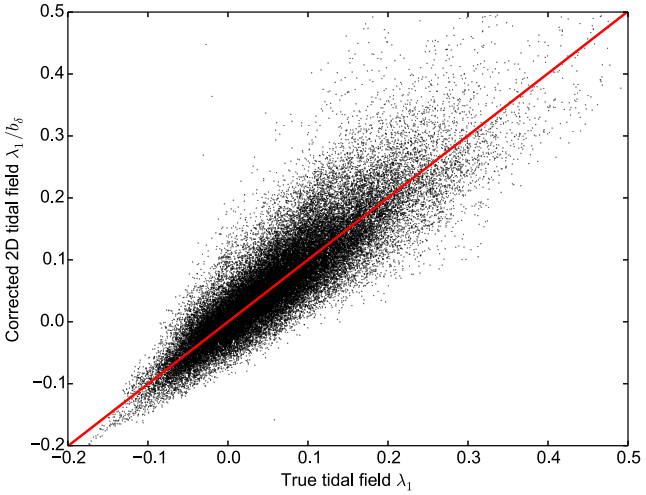

Figure 5. 2D distribution of the values of the principal eigenvalue λ_1 of the true projected tidal tensor (x-axis) and the 2D tidal tensor (y-axis) scaled by the density bias b_δ. b_δ was found by fitting the analogous distribution in the plane of projected matter overdensity ($\delta_{\rm M}$) and projected galaxy overdensity ($\delta_{\rm g}$) to the model $\delta_{\rm g} = b_\delta\,\delta_{\rm M}$. The red solid line shows the best-fitting linear regression, which corresponds to a slope of 1.003 ± 0.002, with a correlation coefficient $r \sim 0.9$, similar to the correlation coefficient found in the plane $\delta_{\rm M} - \delta_{\rm g}$.

The result is shown in Fig. 5, where the black dots correspond to the pairs of values found in the simulation, and the solid red line is the best-fitting zero-intercept linear regression of the points. This fit yields a slope 1.003 ± 0.002, compatible with 1, and a correlation coefficient $r = 0.88$, similar to the value found for the overdensity field. Although our main interest, for the reasons stated in Section 1, is to relate the 2D tidal tensor to the true *projected* tidal forces, we can also use our simulation to explore the connection between the 2D tidal tensor and the transverse components of the true 3D tidal forces (i.e. $\hat{T}_{\rm p}$ in equation 20). In order to do this, we have computed $\hat{T}_{\rm p}$ smoothed with a 3D Gaussian kernel with width $R_G \sim 8\,{\rm Mpc}\,h^{-1}$, corresponding to an angular smoothing scale of $\theta_{\rm sm} = 2^\circ$ at the median redshift of the survey – i.e. the scale used to compute the 2D tidal tensor. We then evaluated this quantity at the position of each galaxy in the mock catalogue located in a range $\Delta z = 0.03$ around the median redshift of the catalogue (i.e. $z \in [0.065, 0.095]$). Finally, we compared the principal eigenvalues of both tensors, as described in the previous paragraph, this time finding a correlation coefficient

$r = 0.58$. Thus, the connection between the 2D tidal tensor and the true 3D tidal forces is less tight than in the case of the projected tidal forces (which is a reasonable result, given the much larger radial smoothing). However, the 2D tidal field as defined here is still a reasonable proxy for the transverse 3D tidal forces at the position of each galaxy around the median redshift.

3.4 Dealing with an incomplete sky coverage

Even though the 2MASS catalogue covered the whole celestial sphere, the Milky Way covers a significant fraction of it, through which the density of detected sources is severely biased by star obscuration and dust extinction. These areas, as well as any region dominated by other observational systematics must therefore be discarded from the analysis, which complicates the application of the method presented here. The main difficulty lies in computing the 2D potential and its derivatives in an incomplete sky: as explained in the previous section, both operations are performed in harmonic space, which involves computing harmonic coefficients of incomplete maps that could be potentially biased. Even solving both problems in real space (e.g. solving Poisson's equation using relaxation techniques) would require assuming something about the values of the density field in the masked pixels, which could significantly bias the estimate of the 2D tidal tensor.

In this work, we have studied two different methods to deal with these issues, which we describe here.

Method I: the overdensity field that we smooth and then use to compute the 2D potential is simply the masked overdensity field, with all masked pixels set to zero.

Method II: in this case, we try to make use of constrained Gaussian realizations (CR from here on) in order to infer the most likely value of the density field in the masked pixels based on the information we have about it outside the mask. Gaussian CRs are used routinely in cosmic microwave background experiments to simplify the computation of the angular power spectrum of maps with small masked areas in them. We will outline the basic procedure used for generating them here, and the reader is referred to Eriksen et al. (2004) for further details.

Writing the full-sky map of the observed density field as a vector $\boldsymbol{d}$ with $n_{\rm pix}$ elements, we can separate it into uncorrelated signal and noise components, $\boldsymbol{d} = \boldsymbol{s} + \boldsymbol{n}$, where unseen (masked) pixels can be modelled as having a very large (infinite) noise component. Assuming both $\boldsymbol{s}$ and $\boldsymbol{n}$ to be Gaussianly distributed, it is easy to prove that the posterior probability distribution for the signal given the data is given by a multivariate normal distribution

$$p(\boldsymbol{s}|\boldsymbol{d}) = N(\boldsymbol{m}, \hat{C}), \tag{21}$$

with mean and covariance given by

$$\boldsymbol{m} = (\hat{S}^{-1} + \hat{N}^{-1})^{-1} \hat{N}^{-1}\, \boldsymbol{d} \tag{22}$$

$$\hat{C} = (\hat{S}^{-1} + \hat{N}^{-1})^{-1}, \tag{23}$$

where $\hat{S} \equiv \langle \boldsymbol{s}\, \boldsymbol{s}^T \rangle$ and $\hat{N} \equiv \langle \boldsymbol{n}\, \boldsymbol{n}^T \rangle$ are the signal and noise covariance matrices (note that the mean $\boldsymbol{m}$ corresponds to a Wiener-filtered version of the data). In our case, we assume that the noise is white (i.e. $\hat{N}$ is diagonal) and we mimic the effect of the mask by making the noise variance infinite in the masked pixels. The inverse noise matrix $\hat{N}^{-1}$ is then easy to calculate in real space and is equal to the inverse noise variance in unmasked pixels and 0 in the masked ones. On the other hand, the signal covariance $\hat{S}$ is given by the two-point correlation function, which makes $\hat{S}^{-1}$ easy to calculate in harmonic space, where it is diagonal. We can then find a maximum likelihood estimator (MLE) for the signal given the data as the mean of the probability distribution above (equation 22). Thus, the combined inverse covariance $(\hat{S}^{-1} + \hat{N}^{-1})^{-1}$ needed to compute $\boldsymbol{m}$ is not diagonal in either real or harmonic space, and the MLE estimator must be computed by numerically solving the linear system:

$$(\hat{S}^{-1} + \hat{N}^{-1})\, \boldsymbol{m} = \hat{N}^{-1}\, \boldsymbol{d}. \tag{24}$$

For this we use the conjugate gradients method, using $\hat{S}$ as a preconditioner.

Finally, we must note that the action of the signal inverse covariance $\hat{S}^{-1}$ was computed by multiplying by the inverse power spectrum of the data in harmonic space. This was estimated as a polynomial fit in logarithmic space to the angular power spectrum of the data computed from the masked overdensity field as

$$C_\ell = \frac{\sum_{m=-\ell}^{\ell} |\tilde{a}_{\ell m}|^2}{(2\ell+1)\, f_{\rm sky}}, \tag{25}$$

where $\tilde{a}_{\ell m}$ are the harmonic coefficients of the masked overdensity field (i.e. with all masked pixels set to zero) and $f_{\rm sky}$ is the fraction of unmasked sky.[5]

The assumption that the signal, noise and data are Gaussianly distributed is not correct for the projected overdensity field, especially at low redshifts due to non-linear clustering. In order to ameliorate this problem, we first transformed the original overdensity field ($\delta_{\rm data}$) into a 'Gaussianized' version of it given by

$$\delta_{\rm Gaussian} = \ln\left[(1+\delta_{\rm data})\sqrt{1+\sigma_\delta^2}\right], \tag{26}$$

where $\sigma_\delta^2 \equiv \langle \delta_{\rm data}^2 \rangle$. Since the overdensity field is known to be well described qualitatively by a lognormal distribution (Coles & Jones 1991, at least at the one-point level), the idea behind this operation is to produce a more Gaussian field by performing an inverse lognormal transformation on the original one. $\delta_{\rm Gaussian}$ and its power spectrum are then used to generate the MLE-CR, which is then transformed into a physical overdensity by inverting equation (26).

Before ending this description, it is worth noting that this procedure yields the maximum-likelihood estimate of the tidal field inside the mask. We can then quantify the errors on this estimate by sampling from the posterior distribution and computing the standard deviation of the samples. Each sample can be drawn by generating two white Gaussian random fields with unit variance, $\boldsymbol{r}_S$ and $\boldsymbol{r}_N$, and solving the modified linear system

$$(\hat{S}^{-1} + \hat{N}^{-1})\, \boldsymbol{s} = \hat{N}^{-1}\, \boldsymbol{d} + \hat{S}^{-1/2} \boldsymbol{r}_S + \hat{N}^{-1/2} \boldsymbol{r}_N. \tag{27}$$

We will use this method to compute the errors in our estimate of the 2D tidal field for the 2MASS galaxy survey.

We make extensive use of direct and inverse spherical harmonic transforms (SHTs) both for generating CRs and for the calculation of the tidal tensor. Unlike in the case of Fourier transforms, direct and inverse SHTs do not cancel each other exactly, and small numerical errors can be generated if many consecutive transforms are applied to a given map, especially towards the poles of the sphere. Although we have verified that these errors are sufficiently small to be essentially negligible for our purposes, we have tried to further

[5] Although this is in general known to be a biased estimator of the angular power spectrum for incomplete skies, we verified that the resulting power spectrum was in good agreement with the one estimated using more sophisticated algorithms [e.g. Chon et al. (2004)].

minimize their effect by using angular coordinates such that the masked areas around the galactic plane occupy the regions close to the poles of our coordinate system, where these errors can be most relevant. Thus, all maps displayed below are shown in galactic coordinates rotated by 90 deg (i.e. the galactic plane runs vertically through the centre of our maps leaving the North and South Galactic Poles to the left and right, respectively).

In order to evaluate the goodness of both methods, we have applied them to our simulated catalogue using the angular mask employed in the analysis of the 2MASS data (see Section 4.1). We then compare the recovered 2D tidal tensor with the true tidal tensor computed without the angular mask. For each method we compute a map containing, for each pixel, the relative error in the estimated tidal tensor eigenvalues, defined as

$$\Sigma_\lambda = \sqrt{\frac{(\lambda_1^t - \lambda_1^r)^2 + (\lambda_2^t - \lambda_2^r)^2}{\langle(\lambda_1^t)^2 + (\lambda_1^t)^2\rangle}}, \tag{28}$$

where λ_i^t is the true i-th eigenvalue (i.e. computed from the unmasked density field), and λ_i^r is the one recovered from the masked map. The ensemble average in the denominator was computed by summing overall pixels in the true map. We then judged the performance of each method by comparing four quantities: the average Σ_λ across the sky, the fraction of the sky where $\Sigma_\lambda > 0.2$ and $\Sigma_\lambda > 0.1$ and the fraction of pixels for which the environment type differs from the one found for the true map. We carried out this exercise for our fiducial smoothing scale and eigenvalue threshold (1° and $\lambda_{\rm th} = 0.05$).

Fig. 6 shows maps of Σ_λ for the two methods, and the quantitative results are summarized in Table 1. Overall the best performance is achieved by method II. We observe a better behaviour than method I due to the ability of the maximum-likelihood CR to infer the value of the density field in the pixels near the edge of the mask, and therefore we used that method in the analysis of the 2MASS data.

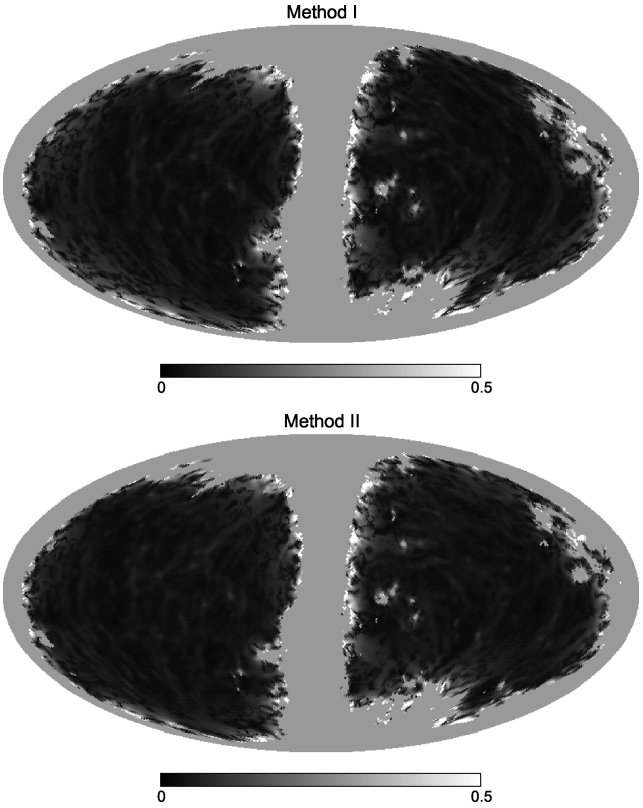

Figure 6. Maps of the error in the eigenvalues of the 2D tidal tensor in each pixel for the two methods described in Section 3.4 to account for the incomplete sky coverage. This uses the simulations described in the text, with the low-latitude mask used for 2MASS, described in Section 4.1. Method II gives smaller errors overall, and we use it as our method of choice for the analysis of the 2MASS data.

Table 1. Comparison between the two methods used to deal with the mask. Even though the two methods show very similar results, method II outperforms method I in the four different metrics, and was therefore our choice in the treatment of the real data.

	Method I	Method II
$\langle\Sigma_\lambda\rangle$	0.074	0.067
per cent area with $\Sigma_\lambda > 0.1$	16.4 per cent	13.3 per cent
per cent area with $\Sigma_\lambda > 0.2$	7.0 per cent	5.9 per cent
per cent misclassifications	5.2 per cent	4.7 per cent

4 THE COSMIC WEB OF 2MASS

In this section, we describe our analysis of the projected tidal structure of the 2MASS survey, which we use to produce a map of the projected tidal forces in the local Universe. As an application of these results, we further study the environmental dependence of the galaxy LF.

4.1 The 2MASS galaxy survey

The 2MASS is a ground-based survey that was carried out between 1997 and 2001 using two twin telescopes located at Mount Hopkins, Arizona and Cerro Tololo, in Chile. It imaged practically the full celestial sphere in the three photometric near-infrared bands J, H and $K_{\rm s}$.[6] The galaxy catalogue used for our analysis is based on the 2MASS extended source catalogue, containing 1647 599 sources, of which more than 98 per cent are galaxies, the remaining 2 per cent being mainly galactic diffuse objects. Of these sources, we omitted all visually confirmed non-extended Galactic sources (flag `vc` = 2), artefacts (`cc_flag` = `a`, `z`), duplicates (`use_src` ≠ 1) and all objects with erroneous or excessively high J, H or $K_{\rm s}$ magnitudes, resulting in a sample containing 1428 756 objects.[7] In the analysis of this sample, we used the $K_{\rm s}$-band 20 mag arcsec^{-2} isophotal fiducial elliptical aperture magnitude (`k_m_k20fe`), which was corrected for Galactic extinction as

$$K_{\rm s} \to K_{\rm s} - A_K, \tag{29}$$

where the $K_{\rm s}$-band correction $A_K = 0.367\,E(B-V)$ was computed from the dust reddening maps of Schlegel, Finkbeiner & Davis (1998).

The main galaxy sample used in this analysis was selected with the aim of obtaining a complete and homogeneous sample. To that extent, we followed the same procedures that were used in Afshordi, Loh & Strauss (2004), Francis & Peacock (2010) and Alonso et al. (2015b), which we summarize here. The two main sources of systematic incompleteness are dust extinction (quantified in terms of A_K above) and stars. We found that a complete and homogeneous sample can be selected for a limiting magnitude $K_{\rm s} = 13.9$ by cutting

[6] All quoted apparent magnitudes correspond to the Vega magnitude system.
[7] Note that this procedure very closely follows the method used by Bilicki et al. (2014) to produce the 2MASS photometric redshift survey.

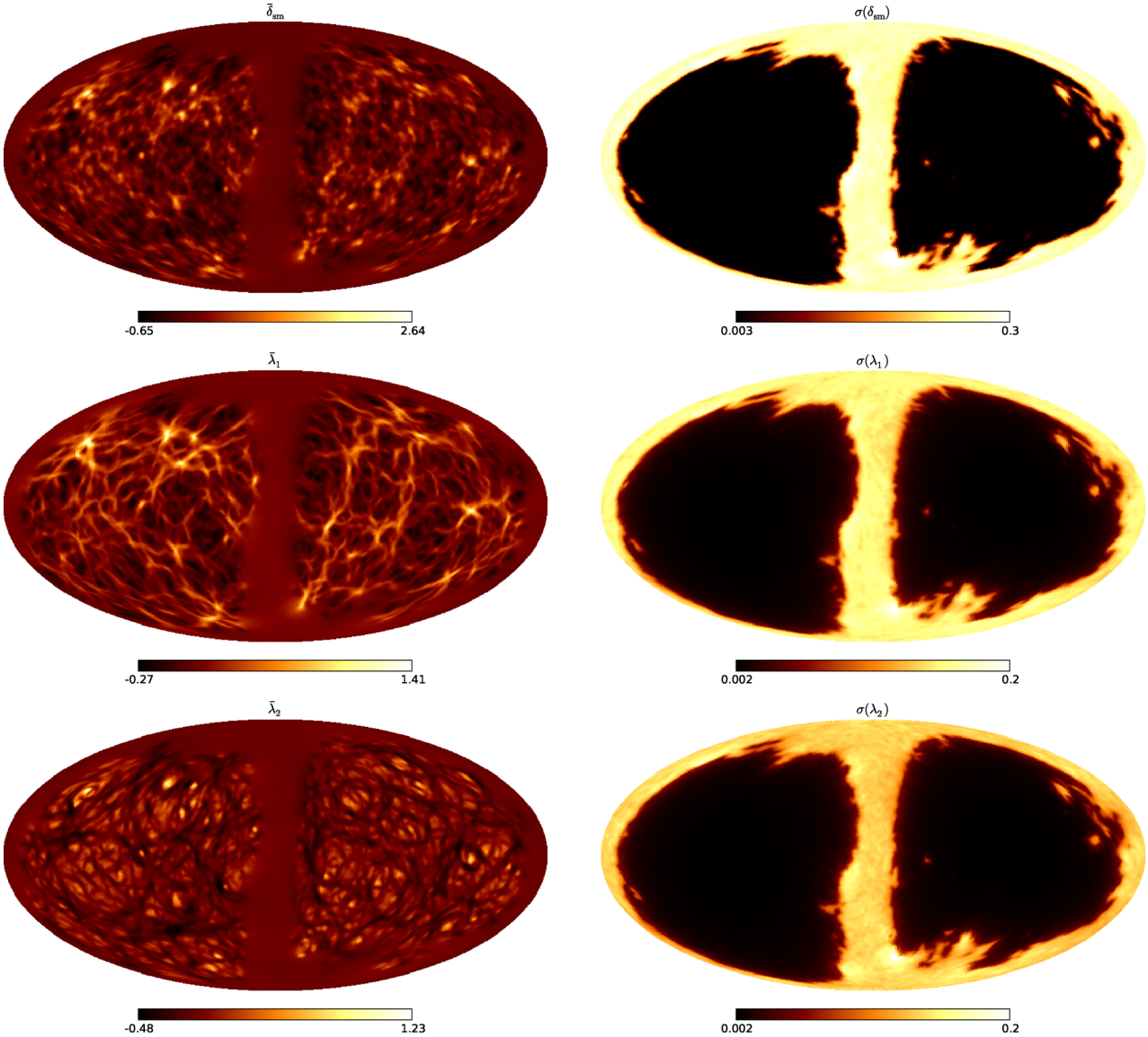

Figure 7. Mean (left column) and standard deviation (right column) of the projected smoothed galaxy density (upper panels) and the corresponding eigenvalues of the 2D tidal tensor (middle and lower panels) as estimated from 1000 CRs of the 2MASS galaxy distribution. Note that the density field is basically unconstrained in masked regions distant from the mask edges, and therefore the mean of the CRs is close to 0 there. A Gaussian smoothing kernel with standard deviation $\theta_s = 1^\circ$ was used.

out all regions of the sky with either $A_K \geq 0.06$ or $\log_{10}(n_{\rm star}/{\rm deg}^2) \geq 3.5$, where $n_{\rm star}$ is the counts of point sources brighter than $K_s = 14$. This procedure reduces the fraction of useable sky to about 69 per cent and constitutes our main galaxy sample, containing 746 733 of the 983 963 galaxies with $K_s \leq 13.9$.

4.2 Results

4.2.1 Estimating the 2D tidal tensor

We estimate the 2D tidal tensor for the galaxy sample described above using method II outlined in Section 3.4. In this approach, we generate a suite of 1000 constrained lognormal realizations of the projected galaxy density field compatible with its statistics in the unmasked regions. Each of these realizations is generated with a HEALPIX resolution `nside` $= 64$ and further smoothed using a Gaussian kernel with standard deviation $\theta_{\rm sm} = 1^\circ$. The smoothed density field is then used to estimate the 2D tidal tensor as well as its eigenvalues and eigenvector in each realization as outlined in Section 3.2. We use this ensemble of estimated 2D tidal fields to evaluate the uncertainty in the measurement of $\hat{t}$. Fig. 7 shows the mean (left column) and standard deviation (right column) of the smoothed density field (upper panels) and the major and minor eigenvalues of the 2D tidal tensor (middle and lower panels) computed from the CRs. The uncertainty in the determination of $\hat{t}$ is very small in regions far from the mask edges, and grows sharply as they are approached. Knowing this uncertainty allows us to define the regions where we trust that estimate enough for the subsequent analyses. We have thus computed the following quantity at each pixel:

$$\tilde{\Sigma}(\hat{\boldsymbol{n}}) = \sqrt{\frac{\sigma^2[\lambda_1(\hat{\boldsymbol{n}})] + \sigma^2[\lambda_2(\hat{\boldsymbol{n}})]}{\langle\bar{\lambda}_1^2 + \bar{\lambda}_2^2\rangle_m}}, \tag{30}$$

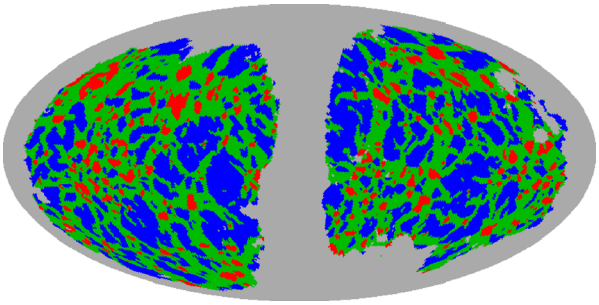

Figure 8. Tidal classification into voids (blue), nexuses (green) and knots (red) of the 2MASS density field. This classification is based on the 1°-smoothed maps of the tidal field eigenvalues shown in Fig. 7, with a threshold $\lambda_{\rm th} = 0.05$.

where $\sigma[\lambda_i(\hat{\boldsymbol{n}})]$ is the uncertainty in the i-th eigenvalue computed from the CRs and $\langle ... \rangle_m$ implies averaging overall unmasked pixels. $\tilde{\Sigma}$ quantifies the magnitude of the error on the tidal tensor eigenvalues normalized by their typical value. In all subsequent analyses, only regions not discarded by the mask described in Section 4.1, and for which $\tilde{\Sigma} < 0.2$ were used, which reduced the available fraction of the sky to 65 per cent. We will use this combined mask in all subsequent analyses unless otherwise stated.

4.2.2 *Statistics of the cosmic web*

As described in Section 2.2.3, our measurement of the 2D tidal field can be used to define different types of environments in terms of the number of eigenvalues found above a given threshold $\lambda_{\rm th}$. For this we use $\lambda_{\rm th} = 0.05$, which we determined by dividing the 2MASS galaxy sample as equally as possible between environments (see Section 2.2.3 and the bottom panel of Fig. 9). The environment classification thus found for 2MASS, using the 2D tidal tensor averaged over the 200 CRs, is shown in Fig. 8.

In order to test the agreement of the statistics of the recovered tidal field with our theoretical expectations, we have compared the sky fraction occupied by the different environments as a function of $\lambda_{\rm th}$ with the results from our simulated galaxy catalogue and the theoretical Gaussian prediction outlined in Appendix B, as shown in Fig. 9. The sky fractions recovered from the data agree well with the results from the simulated catalogue and, qualitatively, follow the same trend predicted by the Gaussian theory. However, the agreement with the latter is much poorer, due to the non-Gaussian nature of the density field on small scales.

4.2.3 *Environmental Dependence of Luminosity Function*

Having access to information about the tidal forces allows us, among other things, to study their influence in the process of galaxy formation and evolution. As an example of this kind of application, we have studied the dependence of the LF on the type of tidal environment. It is well known that more luminous galaxies tend to reside in the highest density regions of the Universe, however no clear dependence has yet been found on tidal or dimensional properties of the environment (Eardley et al. 2015). In order to test this standard prediction in the context of the projected cosmic web, and to further search for other types of environmental dependence we have estimated the $K_{\rm s}$-band LF of 2MASS galaxies in knots, nexuses and voids.

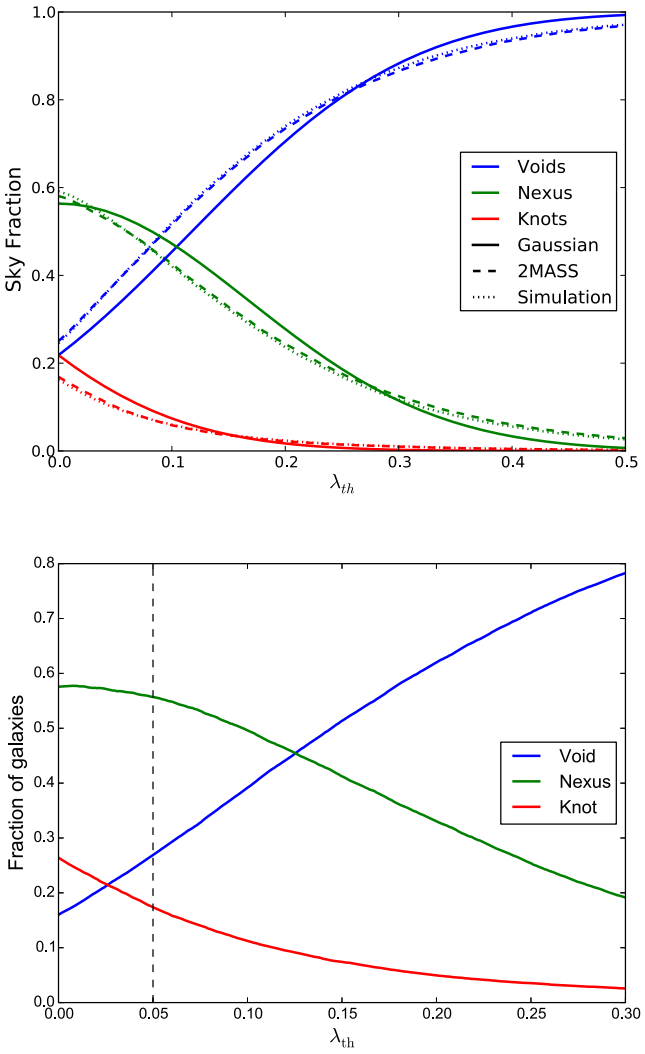

Figure 9. Top panel: sky fraction in the different environments for the 2MASS sample (dashed lines) compared with the simulated catalogue (dotted lines) and the Gaussian theoretical prediction (solid lines) as a function of the eigenvalue threshold and for a smoothing scale $\theta_{\rm s} = 1°$. Blue, green and red lines correspond to voids, nexuses and knots, respectively. Note that the level of disagreement with respect to the Gaussian theoretical prediction is similar to that shown in Fig. 3. Bottom panel: fraction of galaxies in the 2MASS sample found in the three different environments as a function of the eigenvalue threshold. The vertical dashed line shows our choice of $\lambda_{\rm th}$.

Given the redshift z and apparent magnitude m of a galaxy, its absolute magnitude can be computed as

$$M = m - 5\,\log_{10}\left[\frac{d_L(z)}{1\,{\rm Mpc}}\right] - 25 + K(z) + E(z), \qquad (31)$$

where $d_L(z) \equiv (1+z)\,\chi(z)$ is the luminosity distance and $K(z)$ and $E(z)$ are the k-correction and evolution correction, respectively. For the $K_{\rm s}$-band luminosity of 2MASS galaxies, we use the simple forms $K(z) = -6\log_{10}(1+z)$ (Kochanek et al. 2001) and $E(z) = z$ (Blanton et al. 2003), which are accurate enough at the low redshifts ($z \lesssim 0.3$) covered by the survey. For this exercise, we used a sample of 114 930 galaxies with spectroscopic redshifts measured by Sloan Digital Sky Survey (Eisenstein et al. 2011) and the 2MASS redshift survey (Huchra et al. 2012). This sample covers about 5000 deg^2 at galactic latitudes $b \gtrsim 60°$ with a spectroscopic completeness above 90 per cent for $K_{\rm s} < 13.9$ (with the

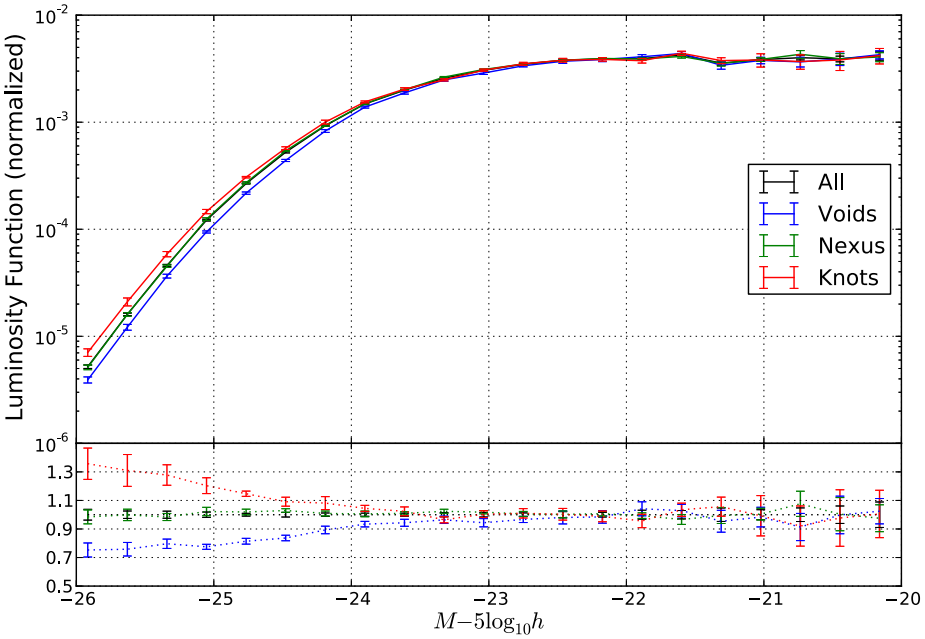

Figure 10. LF of the three environments shown in logarithmic scale. In the bright end, we see a significant overabundance of galaxies in knots with respect to voids as predicted by the standard models of galaxy formation. The colour code is voids (blue); nexuses (green); knots (red). The LFs shown here were normalized to have the same amplitude at magnitudes $M - 5\log_{10}h > -23$. The bottom panel shows the ratios of the void, nexus and knot LFs to the overall LF.

remaining 10 per cent not showing any particular bias in magnitude or position). This sample was used in the calibration of the 2MASS photometric redshift survey (Bilicki et al. 2014), and the spectroscopic redshifts used here were obtained from their publicly available catalogue.

Since the LF $\phi(M)$ is the number density of galaxies per unit interval of absolute magnitude M, the probability of finding the i-th galaxy with absolute magnitude M_i given its redshift z_i in a magnitude-limited sample is given by

$$p(M_i|z_i) = \frac{\phi(M_i)}{\int_{-\infty}^{M_{\rm lim}(z_i)} \phi(M)\,{\rm d}M}, \tag{32}$$

where $M_{\rm lim}(z)$ is the limiting magnitude at redshift z given the magnitude limit of the sample. The joint likelihood of the full sample is then given by the product of this quantity over all the galaxies in the sample. Thus, given a model for the LF, we can find the best-fitting parameters of the model by maximizing $\mathcal{L}$.

Although a Schechter function (Schechter 1976) has often been advocated as a simple and accurate parametrization of the LF, we prefer to use a non-parametric model in order to directly study the environmental dependence as a function of luminosity. Thus, our method of choice is the non-parametric step-wise MLE introduced by (Efstathiou, Ellis & Peterson 1988, EEP from here on). This method models the LF as a step-wise function in a number of magnitude bins,

$$\phi(M) = \sum_{n=1}^{N_{\rm bins}} \phi_n W(M_n - M), \tag{33}$$

where $W(M_n - M)$ is a top-hat function centred around M_n with a width ΔM. Substituting this model in equation (32), we find that the maximum-likelihood parameters ϕ_n must satisfy:

$$\phi_n = \frac{\sum_{m=1}^{N_{\rm bins}} W(M_n - M_m)}{\sum_{i=1}^{N_{\rm g}} \frac{H(M_{\rm lim}(z_i)-M_n)}{\sum_{l=1}^{N_{\rm bins}} \phi_l H(M_{\rm lim}(z_i)-M_l)}}, \tag{34}$$

where $H(x)$ is the integral of $W(x)$. Given an initial guess for the ϕ_n's this equation can then be solved iteratively.

In order to use sample with high-signal-to-noise magnitudes, we only use galaxies brighter than $K_{\rm s} = 13.75$ which, after imposing the mask defined in section 4.2.1 leaves us with a sample of 92 585 galaxies, 22 613 of them in voids, 50 427 in nexuses and 19 545 in knots. $\phi(M)$ was estimated in $N_{\rm bins} = 20$ magnitude bins in the range $M - 5\log_{10}h \in [-26, -20]$, and the statistical errors of these measurements were computed using 10 random jackknife realizations of each galaxy subsample. These jackknife errors were found to be in good agreement with the Poisson uncertainties expected given the galaxy counts in each magnitude bin. Since we expect a smaller environmental dependence in the faint end of the LF, we fix the normalization of the LF in each environment by matching its amplitude to that of the overall LF for magnitudes $M - 5\log_{10}h > -23$ in a χ^2-sense.

The result of this exercise is displayed in Fig. 10: the top panel shows the LF measured in each environment and overall, while the bottom one shows the ratio of the LF in each environment with respect to the measured values across the whole sky. We observe a significant increase in the number density of luminous galaxies in knots with respect to voids, while the nexus LF is perfectly compatible with the overall LF across the whole range of luminosities. As a consistency check, and in order to verify the statistical significance of these differences, we reconstructed the distribution of absolute magnitudes in the data from our estimates of the LF, following Sandage, Tammann & Yahil (1979). To do this, we first compute, for each galaxy at redshift z_i in our sample, the conditional probability distribution $p(M|z_i)$, given in equation (32) in terms of the EEP LF estimated for that sample. We then sum the distributions obtained for all galaxies, normalize the result to unity when integrated over magnitudes, and compare the result with the actual magnitude distribution of the data. The result is shown in Fig. 11: the true magnitude distribution for void galaxies is nicely matched by that assuming the voids LF. However, if the LF estimated for

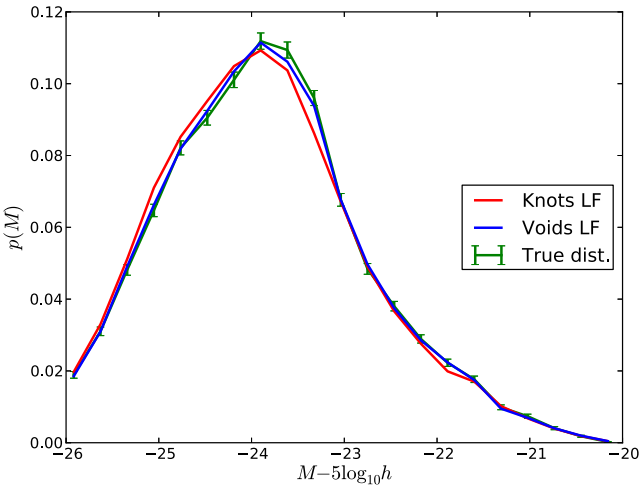

Figure 11. Magnitude distribution computed using the redshift of void galaxies and the EEP LF estimated in voids (blue line), compared to the same quantity computed using the knots LF (but still using the void galaxy redshifts) (red line) and to the true magnitude distribution of void galaxies (green line with Poisson error bars). While the voids LF recovers the true magnitude distribution correctly, the distribution recovered using the knots LF shows significant disagreement. This confirms the statistical significance of the differences found between the LF in voids and knots.

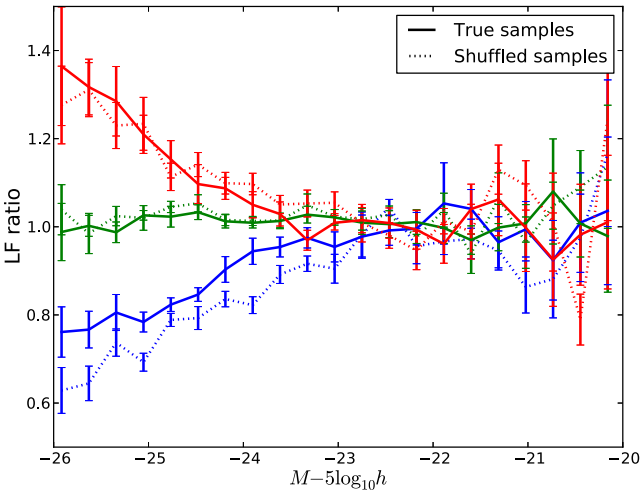

Figure 12. Ratio of the LFs for the true (solid lines) and shuffled (dotted lines) for voids (blue), nexuses (green) and knots (red), to the overall LF. The true and shuffled samples show perfectly compatible LFs, which support the idea that the differences between the three LFs are mainly due to the densities of the different environments, and not to their tidal structure.

knots is used instead, the recovered distribution differs significantly from the true one, which confirms the difference between the two LFs.

Although this is an interesting result, the fact that the three different environment types are associated with different density distributions (which are actually disjoint in the case of knots and voids), makes it difficult to ascertain whether these observed differences are caused by the tidal structure of the environment or merely by its local density, and there are theoretical and empirical reasons to presume that density is the dominant variable (Alonso et al. 2015a; Eardley et al. 2015). In order to address this question, we have carried out an analysis similar to the one used in Eardley et al. (2015). We start by dividing our spectroscopic sample into bins of density. Then, we generated shuffled galaxy samples for each environment type by substituting each galaxy residing in that environment by a random galaxy from the density bin in which it belongs (which will not in general come from the same environment type). We then compute the LF for these shuffled samples and compare them with the corresponding 'true' LF for each environment type. Any differences between both LFs would then be entirely due to tidal effects independent of the environmental density. The result is shown in Fig. 12: in all cases the LFs for the true and shuffled samples are perfectly compatible. Thus, there is no evidence for a dependence of the LF on tidal effects beyond the density dependence.

5 DISCUSSION

In this paper, we have presented a method to reconstruct the transverse tidal forces using the angular position of galaxies in a survey without reliable radial information. The method is based simply on adapting the standard Fourier methods used to estimate the tidal field in 3D data sets to the 2D sphere. We label the object thus recovered the '2D tidal tensor' and show, both in perturbation theory and using a simulated catalogue, that for all scales of interest it can be interpreted as being proportional to the transverse components of the true tidal tensor averaged along the line of sight with the survey window function.

Since the method makes extensive use of operations in harmonic space, special care must be taken when dealing with incomplete sky coverage. In order to deal with this, we make use of constrained lognormal realizations (as described in Section 3.4) in order to find a maximum-likelihood estimate of the tidal field and its uncertainty. We demonstrate the validity of this method by using it on a simulated galaxy catalogue based on an *N*-body simulation. In doing so, we also show that the statistics of the recovered tidal field agree well with the Gaussian prediction (see Appendix B) on large scales, although this agreement breaks down, as expected, on non-linear scales.

We then apply this method to the 2MASS survey and produce a full-sky map of the transverse tidal field, which we make publicly available.[8] The statistics of the recovered tidal field are found to agree quantitatively with our HOD-based simulated catalogue and qualitatively with the Gaussian prediction.

Using the recovered tidal field, we identify three different environment types (knots, nexuses and voids) based on the eigenvalues of the tidal tensor, and compute the LF of galaxies located in each of them. We obtain statistically significant differences in the bright end of the LFs, finding an excess of luminous galaxies in knots with respect to voids. However, we show that this effect is most likely caused by the local density of the environment, and not by its tidal structure. This is in agreement with previous studies (Eardley et al. 2015) and theoretical expectations (Alonso et al. 2015a).

Knowledge of the tidal field also has other interesting applications in cosmology. There is evidence of correlations between the intrinsic shapes and alignments of galaxies (Blazek et al. 2011), which can be a major source of contamination for weak lensing studies. If those correlations were caused by the underlying tidal forces [as suggested by the non-linear alignment – NLA – model (Catelan et al. 2001), as well as recent observations (Pahwa et al. 2015)], prior knowledge about the projected tidal field could potentially reduce the effect of this system, effectively providing a prior on the

[8] http://intensitymapping.physics.ox.ac.uk/2mass_tidal.html

contribution to the shear power spectrum from intrinsic alignments. Note that the projected tidal tensor (which we have shown is well approximated by the 2D tidal tensor) is precisely the quantity that gives rise to this contamination in the NLA model, and therefore the 2D tidal tensor could be used to test the validity of this model explicitly.

The method presented here could therefore be beneficial in the analysis of future deeper photometric surveys, such as DES or LSST. A possible difficulty, in this case, would be the larger projection effects of samples deeper than the one used here, which could significantly degrade the signal-to-noise ratio of the recovered tidal field. A tomographic approach with sufficiently precise photometric redshifts would however ameliorate these effects, and allow for a study of the statistics of the tidal field as a function of redshift.

ACKNOWLEDGEMENTS

We would like to thank Maciej Bilicki, Elisa Chisari, Thibaut Louis and Sigurd Næss for useful comments and discussions. DA is supported by BIPAC, ERC grant 259505 and the Oxford Martin School, and is grateful for the hospitality of Princeton University. BH acknowledges support from the Oxford Astrophysics Summer Student Programme.

REFERENCES

Afshordi N., Loh Y.-S., Strauss M. A., 2004, Phys. Rev. D, 69, 083524
Alonso D., Eardley E., Peacock J. A., 2015a, MNRAS, 447, 2683
Alonso D., Salvador A. I., Sánchez F. J., Bilicki M., García-Bellido J., Sánchez E., 2015b, MNRAS, 449, 670
Appleby S., Shafieloo A., 2014, J. Cosmol. Astropart.Phys., 10, 70
Bardeen J. M., Bond J. R., Kaiser N., Szalay A. S., 1986, ApJ, 304, 15
Berlind A. A., Weinberg D. H., 2002, ApJ, 575, 587
Bilicki M., Jarrett T. H., Peacock J. A., Cluver M. E., Steward L., 2014, ApJS, 210, 9
Blanton M. R. et al., 2003, ApJ, 592, 819
Blazek J., McQuinn M., Seljak U., 2011, J. Cosmol. Astropart.Phys., 5, 10
Bond J. R., Myers S. T., 1996, ApJS, 103, 1
Bond N. A., Strauss M. A., Cen R., 2010a, MNRAS, 406, 1609
Bond N. A., Strauss M. A., Cen R., 2010b, MNRAS, 409, 156
Carretero J., Castander F. J., Gaztañaga E., Crocce M., Fosalba P., 2015, MNRAS, 447, 646
Catelan P., Kamionkowski M., Blandford R. D., 2001, MNRAS, 320, L7
Chen Y.-C. et al., 2015, preprint (arXiv:1509.06376)
Chisari N. E., Mandelbaum R., Strauss M. A., Huff E. M., Bahcall N. A., 2014, MNRAS, 445, 726
Choi E., Bond N. A., Strauss M. A., Coil A. L., Davis M., Willmer C. N. A., 2010, MNRAS, 406, 320
Chon G., Challinor A., Prunet S., Hivon E., Szapudi I., 2004, MNRAS, 350, 914
Coles P., Jones B., 1991, MNRAS, 248, 1
del Castillo G. F. T., 2003, 3-D Spinors, Spin-Weighted Functions and their Applications. Birkhäuser. Springer Int. Publ. AG, Switzerland
Doroshkevich A. G., 1970, Astrophysics, 6, 320
Eardley E. et al., 2015, MNRAS, 448, 3665
Efstathiou G., Ellis R. S., Peterson B. A., 1988, MNRAS, 232, 431
Eisenstein D. J. et al., 2011, AJ, 142, 72
Eriksen H. K. et al., 2004, ApJS, 155, 227
Forero-Romero J. E., Hoffman Y., Gottlöber S., Klypin A., Yepes G., 2009, MNRAS, 396, 1815
Forero-Romero J. E., Contreras S., Padilla N., 2014, MNRAS, 443, 1090
Francis C. L., Peacock J. A., 2010, MNRAS, 406, 2
Górski K. M., Hivon E., Banday A. J., Wandelt B. D., Hansen F. K., Reinecke M., Bartelmann M., 2005, ApJ, 622, 759
Hahn O., Porciani C., Carollo C. M., Dekel A., 2007, MNRAS, 375, 489
Hirata C. M., Seljak U., 2004, Phys. Rev. D, 70, 063526
Hoffman Y., Metuki O., Yepes G., Gottlöber S., Forero-Romero J. E., Libeskind N. I., Knebe A., 2012, MNRAS, 425, 2049
Huchra J. P. et al., 2012, ApJS, 199, 26
Jenkins A., Frenk C. S., White S. D. M., Colberg J. M., Cole S., Evrard A. E., Couchman H. M. P., Yoshida N., 2001, MNRAS, 321, 372
Jing Y. P., Mo H. J., Börner G., 1998, ApJ, 494, 1
Kitaura F.-S., Angulo R. E., Hoffman Y., Gottlöber S., 2012, MNRAS, 425, 2422
Kochanek C. S. et al., 2001, ApJ, 560, 566
Laureijs R. et al., 2011, preprint (arXiv:1110.3193)
Lewis A., Challinor A., Lasenby A., 2000, ApJ, 538, 473
Libeskind N. I., Hoffman Y., Forero-Romero J., Gottlöber S., Knebe A., Steinmetz M., Klypin A., 2013, MNRAS, 428, 2489
Libeskind N. I., Knebe A., Hoffman Y., Gottlöber S., 2014, MNRAS, 443, 1274
LSST Collaboration et al., 2009, preprint (arXiv:0912.0201)
Metuki O., Libeskind N. I., Hoffman Y., Crain R. A., Theuns T., 2015, MNRAS, 446, 1458
Mo H. J., White S. D. M., 1996, MNRAS, 282, 347
Mo H. J., Mao S., White S. D. M., 1999, MNRAS, 304, 175
Nuza S. E., Kitaura F.-S., Heß S., Libeskind N. I., Müller V., 2014, MNRAS, 445, 988
Pahwa I. et al., 2016, MNRAS, 457, 695
Peacock J. A., Smith R. E., 2000, MNRAS, 318, 1144
Planck Collaboration XVI, 2014, A&A, 571, A16
Sandage A., Tammann G. A., Yahil A., 1979, ApJ, 232, 352
Schechter P., 1976, ApJ, 203, 297
Schlegel D. J., Finkbeiner D. P., Davis M., 1998, ApJ, 500, 525
Sheth R. K., Tormen G., 1999, MNRAS, 308, 119
Skrutskie M. F. et al., 2006, ApJ, 131, 1163
Sousbie T., Pichon C., Colombi S., Novikov D., Pogosyan D., 2008, MNRAS, 383, 1655
Springel V., 2005, MNRAS, 364, 1105
The Dark Energy Survey Collaboration, 2005, preprint (astro-ph/0510346)
Vale A., Ostriker J. P., 2004, MNRAS, 353, 189
Wang H., Mo H. J., Yang X., van den Bosch F. C., 2012, MNRAS, 420, 1809
Yan H., Fan Z., White S. D. M., 2013, MNRAS, 430, 3432

SUPPORTING INFORMATION

Additional Supporting Information may be found in the online version of this article:

tidal_2MASS.fits
(http://www.mnras.oxfordjournals.org/lookup/suppl/doi:10.1093/mnras/stw919/-/DC1).

Please note: Oxford University Press is not responsible for the content or functionality of any supporting materials supplied by the authors. Any queries (other than missing material) should be directed to the corresponding author for the article.

APPENDIX A: SPIN-*s* FUNCTIONS ON THE SPHERE

This section introduces a number of mathematical relations regarding spin-s functions in S^2 that will be useful in Appendices B and C.

Let us consider the unit 2-sphere embedded in $\mathbb{R}^3$ and parametrized by the spherical coordinates (θ, φ) as $\boldsymbol{x} = (\sin\theta\,\cos\phi, \sin\theta\,\sin\phi, \cos\theta)$. A rotation by an angle $\psi \in [0, 2\pi)$ around a point $\hat{\boldsymbol{n}}$ on the sphere is defined as a coordinate transformation such that directional vectors of the new coordinates (θ', φ') are rotated with respect to the old ones by an angle ψ within the tangent plane at $\hat{\boldsymbol{n}}$.

Consider now a complex function defined on the unit sphere $f(\hat{\boldsymbol{n}})$. We say that f is a *spin*-s *function* if its transformation law under rotations is $f \to f' = e^{is\psi} f$. Let us now define the so-called spin-raising and spin-lowering differential operators, $\eth$ and $\bar{\eth}$, respectively. They are defined in terms of their actions on a spin-s function ${}_sf$:

$$\eth\, {}_sf \equiv -(\sin\theta)^s(\partial_\theta + i\partial_\varphi/\sin\theta)(\sin\theta)^{-s}\,({}_sf) \tag{A1}$$

$$\bar{\eth}\, {}_sf \equiv -(\sin\theta)^{-s}(\partial_\theta - i\partial_\varphi/\sin\theta)(\sin\theta)^{s}\,({}_sf). \tag{A2}$$

It is possible to prove that, if f is a spin-s function, then $\eth f$ and $\bar{\eth} f$ will be spin-$s+1$ and spin-$s-1$ quantities, respectively (del Castillo 2003).

The simplest functions we can define on the sphere are scalar (spin-0) functions. Such functions can always be expanded in terms of the ordinary spherical harmonics:

$$f(\hat{\boldsymbol{n}}) = \sum_{\ell=0}^{\infty}\sum_{m=-\ell}^{\ell} f_{\ell m}\, Y_{\ell m}(\hat{\boldsymbol{n}}). \tag{A3}$$

By applying the spin-raising and lowering operators, we can define the so-called spin-weighted spherical harmonics ${}_sY_{\ell m}$, defined as

$${}_sY_{\ell m} \equiv \begin{cases} \sqrt{\frac{(\ell-s)!}{(\ell+s)!}}(\eth^s)Y_{\ell m} & 0 \le s \le \ell \\ (-1)^s\sqrt{\frac{(\ell+s)!}{(\ell-s)!}}(\bar{\eth}^{-s})Y_{\ell m} & -\ell \le s \le 0 \\ 0 & \text{otherwise} \end{cases}. \tag{A4}$$

Spin-s functions are then amenable to a harmonic expansion in terms of the spin-s spherical harmonics ${}_sY_{\ell m}$.

The spin-weighted spherical harmonics are related to the Wigner-d rotation matrices through:

$${}_sY_{\ell m}(\theta,\varphi) = (-1)^m\sqrt{\frac{2\ell+1}{4\pi}}e^{im\varphi}d^{\ell}_{-m\,s}(\theta). \tag{A5}$$

The orthogonality of the Wigner-d matrices ($\sum_{m=-\ell}^{\ell} d^{\ell}_{ms}\,(d^{\ell}_{mr})^* = \delta_{sr}$) then implies the following useful relation for the spin-weighted spherical harmonics:

$$\sum_{m=-\ell}^{\ell} |{}_sY_{\ell m}|^2 = \frac{2\ell+1}{4\pi}. \tag{A6}$$

APPENDIX B: GAUSSIAN STATISTICS OF THE 2D TIDAL TENSOR

This appendix discusses and derives the Gaussian prediction for the distribution of the 2D tidal field eigenvalues and the sky fraction occupied by the three different elements of the projected cosmic web.

As outlined in Section 2.2, the 2D tidal tensor is defined in terms of the projected galaxy overdensity as

$$\hat{t} \equiv \hat{H}(\nabla^{-2}_{\hat{\boldsymbol{n}}}\delta), \tag{B1}$$

where $\nabla^{-2}_{\hat{\boldsymbol{n}}} f$ denotes the particular solution of Poisson's equation on the 2-sphere with f as a source, and $\hat{H}$ is the covariant Hessian defined in equation (6). We have further defined the 2D potential $\phi \equiv \nabla^{-2}_{\hat{\boldsymbol{n}}}\delta$, so that $\hat{t} = \hat{H}\phi$.

The 2D tidal tensor can also be written in closed form using the spin-raising and lowering operators $\eth$ and $\bar{\eth}$, introduced in the previous section, as

$$\hat{H}\phi \equiv \frac{1}{2}\begin{pmatrix} \bar{\eth}\eth\phi + \mathrm{Re}(\eth\eth\phi) & \mathrm{Im}(\eth\eth\phi) \\ \mathrm{Im}(\eth\eth\phi) & \bar{\eth}\eth\phi - \mathrm{Re}(\eth\eth\phi) \end{pmatrix}. \tag{B2}$$

The 2D tidal tensor can also be expressed in terms of the covariant derivatives on the sphere as

$$H_{ab}\phi = \frac{\nabla_a\nabla_b\phi}{|\mathbf{e}_a||\mathbf{e}_b|}, \tag{B3}$$

where ∇_a denotes the covariant derivative with respect to the coordinate q_a (either θ or φ), and $\boldsymbol{e}_a \equiv \partial\hat{\boldsymbol{n}}/\partial q_a$ is the Vielbein of the 2-sphere.

Let us focus now on describing the one-point statistics of the 2D tidal tensor under the assumption that the underlying overdensity field is Gaussian. In this case, the probability distribution for $\hat{t}$ will be completely determined by the covariance of its elements:

$$C_{abcd} \equiv \langle t_{ab}t_{cd}\rangle = \frac{\langle\nabla_a\nabla_b\phi\,\nabla_c\nabla_d\phi\rangle}{|\boldsymbol{e}_a||\boldsymbol{e}_b||\boldsymbol{e}_c||\boldsymbol{e}_d|}. \tag{B4}$$

Using the isotropy of the underlying overdensity field, as well as the symmetry properties of the indices [$a \leftrightarrow b$, $c \leftrightarrow d$, $(a,b) \leftrightarrow (c,d)$], we can argue that the tensor in the numerator must be a linear combination of the only three four-index isotropic tensors with equivalent symmetries:

$$\langle\nabla_a\nabla_b\phi\,\nabla_c\nabla_d\phi\rangle = \alpha\, g_{ab}g_{cd} + \beta\, g_{ac}g_{bd} + \gamma\, g_{ad}g_{cb}, \tag{B5}$$

where g_{ab} is the metric of the 2-sphere.

Multiplying this expression above by $g^{ab}g^{cd}$, $g^{ac}g^{bd}$ and $g^{ad}g^{cb}$, and summing over all indices yields a linear system of three equations for the three unknown coefficients α, β and γ. Solving this system, we find that the covariance matrix can be written as

$$C_{abcd} = \frac{1}{8}[(3S_A - 2S_B)\delta_{ab}\delta_{cd} + (2S_B - S_A)(\delta_{ac}\delta_{bd} + \delta_{ad}\delta_{cb})], \tag{B6}$$

where S_A and S_B are the only two second-order rotational invariants of $\hat{t}$:

$$S_A \equiv \langle[\mathrm{Tr}(\hat{t})]^2\rangle = \langle|\bar{\eth}\eth\phi|^2\rangle, \tag{B7}$$

$$S_B \equiv \langle\mathrm{Tr}(\hat{t}^2)\rangle = \frac{1}{2}\left(\langle|\bar{\eth}\eth\phi|^2\rangle + \langle|\eth\eth\phi|^2\rangle\right). \tag{B8}$$

The two ensemble averages $\langle|\bar{\eth}\eth\phi|^2\rangle$ and $\langle|\bar{\eth}\eth\phi|^2\rangle$ can be computed using the harmonic expansion of ϕ:

$$\phi(\hat{\boldsymbol{n}}) \equiv \sum_{\ell=0}^{\infty}\sum_{m=-\ell}^{\ell}\phi_{\ell m}\, Y_{\ell m}(\hat{\boldsymbol{n}}). \tag{B9}$$

Using the definition of the spin-weighted spherical harmonics introduced in Appendix A we obtain:

$$\langle|\bar{\eth}\eth\phi|^2\rangle = \sum_{\ell=0}^{\infty} C^{\phi}_{\ell}\left(\frac{(\ell+1)!}{(\ell-1)!}\right)^2\sum_{m=-\ell}^{\ell}|{}_0Y_{\ell m}|^2, \tag{B10}$$

$$\langle|\eth\eth\phi|^2\rangle = \sum_{\ell=0}^{\infty} C^{\phi}_{\ell}\frac{(\ell+2)!}{(\ell-2)!}\sum_{m=-\ell}^{\ell}|{}_2Y_{\ell m}|^2 \tag{B11}$$

where we have defined the power spectrum of the 2D potential $\langle\phi_{\ell m}\phi^*_{\ell' m'}\rangle \equiv C^{\phi}_{\ell}\delta_{\ell\ell'}\delta_{mm'}$. Using the relation between the harmonic coefficients of the 2D potential and the projected density field ($\delta_{\ell m} = -\ell(\ell+1)\phi_{\ell m}$) as well as the orthogonality relation (equation A6), we finally obtain:

$$\sigma^2_{\delta} \equiv \langle|\bar{\eth}\eth\phi|^2\rangle = \sum_{\ell=0}^{\infty}\frac{2\ell+1}{4\pi}C^{\delta}_{\ell}, \tag{B12}$$

$$\tilde{\sigma}^2_{\delta} \equiv \langle|\eth\eth\phi|^2\rangle = \sum_{\ell=0}^{\infty}\frac{2\ell+1}{4\pi}C^{\delta}_{\ell}\left[\frac{(\ell+2)(\ell-1)}{\ell(\ell+1)}\right]. \tag{B13}$$

Note that σ_δ^2 is the variance of the projected overdensity field. Furthermore, in the flat-sky approximation, where only the highest multipoles ($\ell \gg 1$) contribute to the total power, $\tilde{\sigma}_\delta \simeq \sigma_\delta$, and thus $S_B \simeq S_A = \sigma_\delta^2$.

Collecting the three independent terms of the 2D tidal tensor into a 3D vector: $\boldsymbol{t} \equiv (t_{\theta\theta}, t_{\phi\phi}, t_{\theta\phi})$, the covariance matrix can be written as a 3×3 symmetric matrix in terms of σ_δ^2 and $\tilde{\sigma}_\delta^2$:

$$\hat{C} \equiv \langle \boldsymbol{t}\, \boldsymbol{t}^T \rangle = \frac{1}{8} \begin{pmatrix} 2\sigma_\delta^2 + \tilde{\sigma}_\delta^2 & 2\sigma_\delta^2 - \tilde{\sigma}_\delta^2 & 0 \\ 2\sigma_\delta^2 - \tilde{\sigma}_\delta^2 & 2\sigma_\delta^2 + \tilde{\sigma}_\delta^2 & 0 \\ 0 & 0 & \tilde{\sigma}_\delta^2 \end{pmatrix}. \tag{B14}$$

In order to derive the probability distribution for the eigenvalues of $\hat{t}$, we follow the procedure used in Alonso et al. (2015a). The probability distribution for the vector $\boldsymbol{t}$ is given by a multivariate Gaussian:

$$p(\boldsymbol{t}) \prod_{A=1}^{3} \mathrm{d}t_A = \frac{\exp\left[-\frac{1}{2}\boldsymbol{t}^T \hat{C}^{-1} \boldsymbol{t}\right]}{\sqrt{(2\pi)^3 \det(\hat{C})}} \prod_A \mathrm{d}t_A. \tag{B15}$$

This can be simplified by defining the rescaled variables:

$$\nu \equiv \frac{t_1 + t_2}{\sigma_\delta}, \quad \rho \equiv \frac{t_1 - t_2}{2\tilde{\sigma}_\delta}, \quad \tau \equiv \frac{t_3}{\tilde{\sigma}_\delta}, \tag{B16}$$

which diagonalize the covariance matrix, yielding

$$p(\boldsymbol{t}) \prod_{A=1}^{3} \mathrm{d}t_A = \frac{8\, e^{-(\nu^2 + 8\rho^2 + 8\tau^2)/2}}{(2\pi)^{3/2} \sigma_\delta \tilde{\sigma}_\delta^2} \prod_A \mathrm{d}t_A. \tag{B17}$$

On the other hand, the volume element $\prod_A \mathrm{d}t_A$ in the space of 2×2 symmetric matrices can be written in terms of their two eigenvalues, λ_1 and λ_2 and the angle defining the 2D rotation that diagonalizes it (Bardeen et al. 1986):

$$\prod_A \mathrm{d}t_A = |\lambda_1 - \lambda_2|\, \mathrm{d}\lambda_1 \mathrm{d}\lambda_2 \frac{\mathrm{d}\phi}{4}, \tag{B18}$$

where the factor of $1/4$ accounts for the two different orderings of the eigenvalues and the overall sign defines the orientation of the eigenvectors. Choosing the ordering $\lambda_1 > \lambda_2$ introduces a factor of 2. Expressing λ_1 and λ_2 in terms of ν and ρ, and integrating the irrelevant angular part, we finally obtain the distribution:

$$p(\nu, \rho)\, \mathrm{d}\nu\, \mathrm{d}\rho = 8\, \rho\, e^{-4\rho^2}\, \mathrm{d}\rho\, \frac{e^{-\nu^2/2}}{\sqrt{2\pi}}\, \mathrm{d}\nu. \tag{B19}$$

The ordering $\lambda_1 > \lambda_2$ has the effect of reducing the dynamical range of ρ to $\rho > 0$, and the integration limits for ν are determined by the environment type, defined by the eigenvalue threshold $\lambda_{\rm th}$ and the number of eigenvalues above the threshold (α). In general, we can write $f_1(\alpha, \rho) < \nu - \nu_{\rm th} < f_2(\alpha, \rho)$, with $\nu_{\rm th} \equiv 2\lambda_{\rm th}/\sigma_\delta$ and

$$f_1(\alpha, \rho) = \begin{cases} -\infty & \alpha = 0\,(\text{void}) \\ -2\frac{\tilde{\sigma}_\delta}{\sigma_\delta}\rho & \alpha = 1\,(\text{nexus}) \\ 2\frac{\tilde{\sigma}_\delta}{\sigma_\delta}\rho & \alpha = 2\,(\text{knot}) \end{cases}, \tag{B20}$$

$$f_2(\alpha, \rho) = \begin{cases} -2\frac{\tilde{\sigma}_\delta}{\sigma_\delta}\rho & \alpha = 0\,(\text{void}) \\ 2\frac{\tilde{\sigma}_\delta}{\sigma_\delta}\rho & \alpha = 1\,(\text{nexus}) \\ \infty & \alpha = 2\,(\text{knot}) \end{cases}. \tag{B21}$$

The sky fraction for the three types of environment can then be computed by integrating the probability distribution in equation (B19) with the corresponding integration limits for ν:

$$F_V(\alpha, \lambda_{\rm th}) = \frac{8}{\sqrt{2\pi}} \int_0^\infty \mathrm{d}\rho \int_{\nu_{\rm th} + f_1(\alpha,\rho)}^{\nu_{\rm th} + f_2(\alpha,\rho)} \mathrm{d}\nu\, \rho\, e^{-(\nu^2 + 8\rho^2)/2}. \tag{B22}$$

Note that this integral can be solved analytically in terms of error functions, but we omit the resulting cumbersome expression.

APPENDIX C: RELATION BETWEEN THE 2D TIDAL TENSOR AND THE PROJECTED TIDAL FORCES

Using the flat-sky approximation, we have shown in Section 2.2.2 that the 2D tidal tensor, as defined in Section 2.2.1 can be interpreted, on sufficiently small scales, as being proportional to the gravitational tidal forces in the transverse (angular) directions averaged along the line of sight with the survey selection function. The aim of this Appendix is to present a more rigorous proof of this relation in the full-sky limit, as well as to provide the formulas relating the 2D tidal tensor and the underlying matter perturbations.

As shown in Appendix B, the components of the 2D tidal tensor can be related to the two complex quantities

$$t^{(0)}(\hat{\boldsymbol{n}}) \equiv \bar{\eth}\eth \left[\nabla_{\hat{\boldsymbol{n}}}^{-2} \left(\int_0^\infty \mathrm{d}\chi\; w(\chi)\, \delta^s(\chi \hat{\boldsymbol{n}})\right)\right], \tag{C1}$$

$$t^{(2)}(\hat{\boldsymbol{n}}) \equiv \eth\eth \left[\nabla_{\hat{\boldsymbol{n}}}^{-2} \left(\int_0^\infty \mathrm{d}\chi\; w(\chi)\, \delta^s(\chi \hat{\boldsymbol{n}})\right)\right], \tag{C2}$$

where $\delta^s(\boldsymbol{x})$ is the observed density field in redshift space. On the other hand, the projected tidal tensor (i.e. the tidal forces along the transverse directions averaged along the line of sight) is given by the analogous quantities:

$$\tilde{t}^{(0)}(\hat{\boldsymbol{n}}) \equiv \int_0^\infty \mathrm{d}\chi\; w(\chi) \frac{\bar{\eth}\eth \Phi(\chi \hat{\boldsymbol{n}})}{\chi^2}, \tag{C3}$$

$$\tilde{t}^{(2)}(\hat{\boldsymbol{n}}) \equiv \int_0^\infty \mathrm{d}\chi\; w(\chi) \frac{\eth\eth \Phi(\chi \hat{\boldsymbol{n}})}{\chi^2}, \tag{C4}$$

where Φ is the Newtonian potential normalized so that $\nabla^2 \Phi = \delta$, with δ the real-space density field. Let us focus, for the moment, on the trace of the two tidal tensors, given by $t^{(0)}$ and $\tilde{t}^{(0)}$.

We start by computing the harmonic coefficients of both quantities, given by

$$t_{\ell m}^{(0)} \equiv \int \mathrm{d}\hat{\boldsymbol{n}}\; Y_{\ell m}^*(\hat{\boldsymbol{n}})\, t^{(0)}(\hat{\boldsymbol{n}}), \tag{C5}$$

(and likewise for $\tilde{t}^{(0)}$). We can relate $t_{\ell m}^{(0)}$ to the matter density perturbations by doing the following.

(i) First, expand δ_s in equation (C1) in terms of its Fourier coefficients, and use the plane-wave expansion

$$e^{i\boldsymbol{k}\boldsymbol{x}} = \sum_{\ell=0}^{\infty} 4\pi i^\ell\, j_\ell(k\chi) \sum_{m=-\ell}^{\ell} Y_{\ell m}(\hat{\boldsymbol{n}}) Y_{\ell m}^*(\hat{\boldsymbol{n}}_k), \tag{C6}$$

where $\boldsymbol{x} \equiv \chi \hat{\boldsymbol{n}}$, $\hat{\boldsymbol{n}}_k$ is the unit vector in Fourier space and $j_\ell(x)$ is the order-ℓ spherical Bessel function of the first kind.

(ii) Apply the operator $\bar{\eth}\eth \nabla_{\hat{\boldsymbol{n}}}^{-2}$ on the spherical harmonic $Y_{\ell m}(\hat{\boldsymbol{n}})$

$$\bar{\eth}\eth \nabla_{\hat{\boldsymbol{n}}}^{-2} Y_{\ell m}(\hat{\boldsymbol{n}}) = Y_{\ell m}(\hat{\boldsymbol{n}}). \tag{C7}$$

(iii) Relate the Fourier coefficients of the observed overdensity field δ^s to the real-space density perturbations:

$$\delta_k^s\, j_\ell(k\chi) \longrightarrow b\, \delta_k \left[j_\ell(k\chi) - \beta j_\ell''(k\chi)\right], \tag{C8}$$

where b is the linear galaxy bias and β is the redshift distortion parameter.

(iv) Define the harmonic coefficients of δ_k as

$$\delta_{\ell m}(k) \equiv \int d\hat{\boldsymbol{n}}_k Y^*_{\ell m}(\hat{\boldsymbol{n}}_k)\, \delta_{\boldsymbol{k}}. \tag{C9}$$

Finally, we obtain the following relation between $t^{(0)}_{\ell m}$ and $\delta_{\ell m}(k)$:

$$t^{(0)}_{\ell m} = b\, \frac{4\pi i^\ell}{(2\pi)^{3/2}} \int_0^\infty \mathrm{d}k\, k^2\, \delta_{\ell m}\, w_\ell(k), \tag{C10}$$

with

$$w_\ell(k) \equiv \int_0^\infty \mathrm{d}\chi\ \left[j_\ell(k\chi) - \beta\, j''_\ell(k\chi)\right] w(\chi). \tag{C11}$$

Following analogous steps for $\tilde{t}^{(0)}_{\ell m}$ yields a similar relation:

$$\tilde{t}^{(0)}_{\ell m} = \frac{4\pi i^\ell}{(2\pi)^{3/2}} \int_0^\infty \mathrm{d}k\, k^2\, \delta_{\ell m}\, \tilde{w}_\ell(k), \tag{C12}$$

with

$$\tilde{w}_\ell(k) \equiv \int_0^\infty \mathrm{d}\chi\ \frac{\ell(\ell+1)}{(k\chi)^2}\, j_\ell(k\chi)\, w(\chi). \tag{C13}$$

Thus, as was shown in the flat-sky case, the differences between the 2D tidal tensor and the projected tidal forces, besides the linear galaxy bias acting as a proportionality constant, are encapsulated in the different window functions w_ℓ and $\tilde{w}_\ell$ above.

Fig. C1 shows both window functions for different values of ℓ for the 2MASS selection function using an RSD parameter $\beta = 0.46$ (Alonso et al. 2015b). As is evident, on small scales (large-ℓ) the two functions are almost equivalent, and in this case the 2D tidal tensor can be safely interpreted as describing the average tidal forces in the transverse directions.

Similar relations can be derived for $t^{(2)}$ and $\tilde{t}^{(2)}$ by following the same steps outlined above, with the exception that, since they are spin-2 quantities, their harmonic coefficients must be computed using the spin-weighed spherical harmonics (equation A4). The resulting expressions are

$$t^{(2)}_{\ell m} = b\, \frac{4\pi i^\ell}{(2\pi)^{3/2}} \int_0^\infty \mathrm{d}k\, k^2\, \delta_{\ell m}\, w^{(2)}_\ell(k), \tag{C14}$$

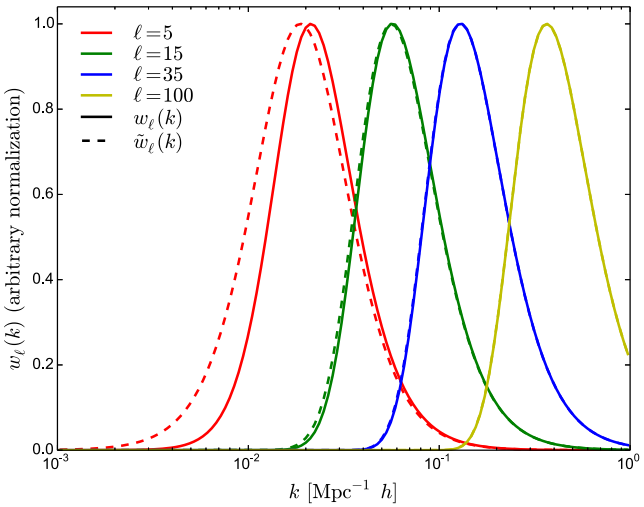

Figure C1. Window functions $w_\ell(k)$ and $\tilde{w}_\ell(k)$ defined in equations (C10) and (C12) for the 2MASS selection function and different values of the multipole order ℓ. The difference between the 2D tidal tensor and the projected tidal forces is effectively encapsulated in the differences between the two functions. These differences become negligible by $\ell \simeq 15$, and hence, for most scales of interest, it is safe to interpret the 2D tidal tensor as describing the transverse tidal forces averaged along the line of sight.

$$\tilde{t}^{(2)}_{\ell m} = \frac{4\pi i^\ell}{(2\pi)^{3/2}} \int_0^\infty \mathrm{d}k\, k^2\, \delta_{\ell m}\, \tilde{w}^{(2)}_\ell(k), \tag{C15}$$

with

$$\begin{pmatrix} w^{(2)}_\ell(k) \\ \tilde{w}^{(2)}_\ell(k) \end{pmatrix} \equiv \left[\frac{(\ell+2)(\ell-1)}{\ell(\ell+1)}\right]^{1/2} \begin{pmatrix} w_\ell(k) \\ \tilde{w}_\ell(k) \end{pmatrix}. \tag{C16}$$

This paper has been typeset from a TEX/LATEX file prepared by the author.